Journal Pre-proof

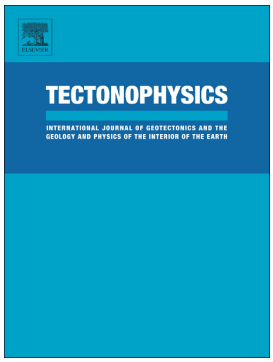

Frictional properties of basalt experimental faults and implications for volcano-tectonic settings and geo-energy sites

Piercarlo Giacomel, Roberta Ruggieri, Marco M. Scuderi, Elena Spagnuolo, Giulio Di Toro, Cristiano Collettini

PII: S0040-1951(21)00167-0

DOI: https://doi.org/10.1016/j.tecto.2021.228883

Reference: TECTO 228883

To appear in: *Tectonophysics*

Received date: 5 August 2020

Revised date: 13 April 2021

Accepted date: 19 April 2021

Please cite this article as: P. Giacomel, R. Ruggieri, M.M. Scuderi, et al., Frictional properties of basalt experimental faults and implications for volcano-tectonic settings and geo-energy sites, *Tectonophysics* (2021), https://doi.org/10.1016/j.tecto.2021.228883

Frictional properties of basalt experimental faults and implications for volcano-tectonic settings and geo-energy sites

Piercarlo Giacomel[1,*] piercarlo.giacomel@uniroma1.it, Roberta Ruggieri[1], Marco M. Scuderi[1], Elena Spagnuolo[2], Giulio Di Toro[2,3], and Cristiano Collettini[1,2]

[1]Dipartimento di Scienze della Terra, Sapienza Università di Roma, Piaz. Aldo Moro 5, Rome

[2]Istituto Nazionale di Geofisica e Vulcanologia, Via di Vigna Murata 605, Rome, Italy

[3]Dipartimento di Geoscienze, Università degli Studi di Padova, Via G. Gradenigo 6, Padua, Italy

[*]Corresponding author.

0. ABSTRACT

We performed a suite of experiments aimed at examining the frictional properties of unaltered basalts at conditions considered to be representative of slip at shallow depths in volcano-tectonic environments and *in-situ* geo-energy basaltic sites. Scientific drilling and field studies on exhumed subsurface faults and fractures analogues suggest that, frictional sliding in basalts can occur in shear zones within a volume of wear debris or along localized joint surfaces. To illuminate how microstructural heterogeneities effect the nucleation of slip instabilities into basalts, we sheared simulated fault gouge and bare rock surfaces at low normal stresses (4 to 30 MPa) at ambient temperature, under room-dry and wet conditions. We performed velocity steps (0.1-300 μm/s) and slide-hold-slides (30-3000 s holds) to determine the frictional stability and healing properties of basalts. In all the tests, we observed high friction coefficient associated with important frictional restrengthening. Overall, our results show that microstructural heterogeneities strongly affect the friction velocity dependence of basalts: while for normal stresses ≥ 10 MPa, shear localization accompanied by cataclasis and grain size reduction favors the transition to velocity weakening behavior of powdered samples, on bare surfaces gouge production during shearing promotes a transition to a velocity strengthening behavior. Our results imply that at the tested conditions, friction instabilities may promptly nucleate in shear zones where deformation within (unaltered) basaltic gouge layers is localized, such as those located along volcanic flanks, while joint surfaces characterized by rough rock-on-rock contacts are less prone to unstable slip, which is suppressed at velocities ≥ 10 μm/s.

KEY WORDS

- Unaltered basalts
- Strong faults
- Heterogeneous fault microstructure
- Frictional stability analysis
- Fault slip modes

1. INTRODUCTION

The frictional properties of fault rocks exert a primary control on fault slip behavior (*Brace and Byerlee*, 1966). Multiple data sources support the frictionally strong nature of a broad gamut of seismically active faults, with the static coefficient of Coulomb friction μ in the range 0.6-0.85 (e.g., *Byerlee*, 1978; *Collettini and Sibson*, 2001*; Scholz*, 2000) and high frictional healing values, which allow the rapid recovery of shear strength required for repeated fault reactivations (*Carpenter et al.*, 2014; *Marone*, 1998b). However, several lines of evidence suggest that fault frictional and microstructural heterogeneities may result in complex slip behavior (e.g., *Ben-Zion*, 2001; *Boatwright and Cocco*, 1996; *Collettini et al.*, 2019; *Di Stefano et al.*, 2011; *Kaneko et al.*, 2010; *Niemeijer and Vissers*, 2014, and many others), which can be captured by variations in rate and state friction constitutive parameters.

In the last few decades, the seismic and landslide hazard potential related to volcano-tectonic environments have raised the burning necessity to delve into the mechanisms of slip instability nucleation into basalts also at shallow depths. Reported examples of active volcano-tectonics include the Kilauea and Mauna Loa basaltic volcanoes in Hawaii, where rates of shear failures are mainly controlled by local stress changes associated to magmatic intrusions or eruptive activities (e.g., *Aki and Ferrazzini*, 2001): here the observed shallow Mw ≤ 3 seismicity clustered at 0 -3 km bgl (below ground level) beneath the summit calderas and along the rift zones (*Klein et al.*, 1987; *Klein*, 2016; *Lin and Okubo*, 2020; *Lengliné et al.*, 2008; *Lockwood et al.*, 1987). Submarine evidence and seismic surveys have also found the presence of sand-sized debris where deformation was accommodated via shallow landslides cutting the Hawaiian volcano flanks. Some of these deposits are mainly derived from fragmented lava flows, which are considered the dominant rock type in the upper first km of the Mauna Loa's submarine slope section (*Denlinger and Morgan*, 2014; *Garcia and Davis*, 2001). Striking similarities characterize other active volcano-tectonic settings, such as the Mt. Etna basaltic stratovolcano in Italy, where many of the shallow earthquakes nucleate and/or propagate in basaltic lava flows located beneath the central summit area and along the eastern flank of the volcano (*Azzaro et al.*, 2017; *Branca et al.*, 2011; *Villani et al.*, 2020). The latter represents a relevant source of hazard since it also encompasses a densely urbanized area (*Azzaro et al.*, 2013). A clear evidence of fault reactivations along the eastern flank is the shallow seismogenic layer located between the ground surface and 5 km depth along the Pernicana-Provenzana Fault system, that enucleated up to Mw 4.2 subsurface earthquakes in basalts during the 1981-1988 seismic sequence (*Alparone et al.*, 2013; *Azzaro et al.*, 2017). Although it is not uncommon that synmagmatic fault zones can present pervasive alteration (i.e., smectites) and mineralization (i.e., calcite and zeolite) of the primary basaltic fault gouge mineralogy (*Khodayar and Einarsson*, 2002; *Kristmannsdóttir*, 1979; *Reidel et al.*, 2013; *Walker et al.*, 2012, 2013a, 2013b), in some cases shear zones are localized in unaltered volcanic fault gouge. A good example is represented by the plagioclase-rich wear debris formed along the margins of the Mount St. Helens lava domes, in response to persistent stick-slip events at < 1 km depth coupled with volcanic extrusion (*Cashman et al.*, 2008; *Iverson et al.*, 2006; *Kendrick et al.*, 2012; *Moore et al.*, 2008).

Understanding the frictional behavior of unaltered basalt bare surfaces is of strategic importance in basalt-hosted geo-reservoirs and/or caprocks for the safe *in-situ* carbon geological sequestration or for the reinjection of wastewater byproducts from geothermal power plants. In some of the selected regions, such as the Wallula Basalt Sequestration and the CarbFix pilot projects (*Gislason et al.*, 2010; *Kelemen et al.*, 2019; *McGrail et al.*, 2011; *Snæbjörnsdóttir et al.*, 2020), the majority of basalts are low-altered and far from the local high-temperature geothermal systems, so that temperature reaches up to 35°C in the main target aquifers, located respectively at ~ 800 m and 500 m depth (*Alfredsson et al.*, 2013; *McGrail et al.*, 2006). Furthermore, basaltic lava flows capping a storage reservoir normally exhibit cooling columnar joints and (micro) fractures that can potentially affect the integrity and stability of the fluid repositories (e.g., *Goldberg et al.*, 2010). As a matter of fact, pervasive joint sets can act as preexisting weakness surfaces inside the intact rock and consequently be reactivated during fluid injection in tectonically active areas (*Hatton et al.*, 1994). Outcrop studies conducted by *Walker et al.* (2012, 2013b) on exhumed subsurface (0 - 3 km bgl) faults and fractures within continental flood basalts, confirmed the occurrence of reactivated unaltered basalt joints, leading to fault-zone development and possibly seismicity.

To date, although a concerted effort has been done to characterize the frictional properties of intrusive rocks like gabbros (*Cox*, 1990; *He et al.*, 2006, 2007; *Marone and Cox*, 1994; *Mitchell et al.*, 2015), friction stability data on its extrusive counterpart (i.e., basalts) are still limited. To our knowledge, measurements of the friction velocity dependence of basalts were carried out by *Zhang et al.* (2017) on unaltered basalt gouge having a particle size, Φ, < 74 μm, at effective normal stress, σ'_n, of 45 – 51 MPa under hydrothermal conditions, and by *Ikari et al.* (2020), on both altered basalt gouge with Φ < 125 μm and bare surfaces finished with #60-grit, at room temperature and σ'_n = 25 MPa.

In order to investigate the possible modes of slip that may arise from differences in fault microstructures, we investigated the frictional properties and the friction velocity dependence of unaltered basalts simulating deformation along localized rough joint surfaces, i.e., bare rock surfaces, and shear zones containing fault gouge, i.e., powdered material. The results presented in this study, obtained under low normal stresses (≤ 30 MPa), room-dry and wet conditions at ambient temperature, allow us to fill a knowledge gap found in the literature and carry important implications for *(i)* the refinement of local seismic and landslide hazard evaluation in volcanic flanks and edifices and *(ii)* the integrity and stability of basalt-hosted geo-energy sites.

2. MATERIALS AND METHODS

Selected specimens are trachybasalts from Mount Etna (Italy), with an initial density of 2980 ± 10 kg/m^3 and a connected porosity of ~ 6%, measured with the Helium pycnometer Accu Pyc II 1340 installed at the Istituto Nazionale of Geofisica and Vulcanologia (INGV) in Rome (Italy). Bulk-rock chemical and mineralogical analysis were performed using X-ray fluorescence (XRF) and X-Ray powder diffraction (XRPD) at the laboratories located at the Dipartimento di Geoscienze of Università di Padova (Padua) and are reported in Supplementary Figures S1 and S2. Etnean basalts are typical lava flow basalts with a porphyric texture (Figure S3 Suppl. Mat.) with phenocrysts showing no discernable preferred alignment. The primary minerals consist in mm-sized phenocrysts of olivine, clinopyroxene (augite), plagioclase and Fe-Ti oxides, in a completely crystallized groundmass (~ 60% vol on average) with the same mineralogy. The heterogenous spatial distribution of the phenocrysts in basaltic lava flows explains the variable percentage of phenocrystals among different specimens. The relative abundance of the olivine, plagioclase, and pyroxenes, which are the most efficient sources of divalent cations for mineral carbonation, renders Etnean basalts also a suitable natural analogue for CO_2 sequestration into basaltic rocks (e.g., *Kelemen et al. 2019*).

2.1 Biaxial deformation experiments

To simulate natural fault gouges, intact fragments of the starting protolith were crushed in a disk mill and hand-sieved to get powders with a grain size < 125 μm. The grain size fraction of starting basalt revealed a high concentration of fine material resulting in about 50% of the volume characterized by a particle size < 20 μm (Figure S4, Suppl. Mat.). To simulate fault surfaces, basalt slabs were carefully cut to produce samples of 4X4 cm^2 nominal area and approximately 0.8 – 1.2 cm thick. In this arrangement the bare surfaces were polished flat with a precision grinder better than 0.1 mm and then hand roughened with #80 grit SiC abrasive powder and water on a glass plate.

We performed laboratory friction experiments in a servo-controlled biaxial deformation apparatus, BRAVA (Brittle Rock deformation Versatile Apparatus; *Collettini et al.*, 2014), hosted at the HP-HT Laboratory of the INGV in Rome, Italy. The apparatus is equipped with a fast-acting hydraulic servo-controlled ram that was used to apply and maintain constant normal stress (σ_n) on the simulated fault zone via a load-feedback loop control system. Likewise, a servo-controlled vertical ram was used to apply shear stress (τ). The vertical piston was controlled in displacement-feedback mode, in which the ram was advanced at a constant displacement rate. Applied forces were measured using load cells with 0.03 kN resolution over a maximum force of 1.5 MN, that are calibrated regularly. Displacements were measured to ± 0.1 μm via Linear Variable Displacement Transfomers (LVDTs) throughout the experiments. Load point displacement measurements were corrected for the stiffness of the apparatus, with nominal values of 386.12 kN/mm for the horizontal frame and of 359.75 kN/mm for the vertical frame.

We used the double direct-shear configuration to perform experiments on fault gouge (Figure 1b). This experimental configuration consists of two parallel layers of simulated fault gouge placed in between

three grooved steel blocks. The grooves are 0.8 mm in height and spaced 1 mm and they ensure shear localization within the fault gouge. For each experiment, the two gouge layers were produced using leveling jigs to obtain a uniform layer thickness of 5 mm before the samples were loaded. These layers have a 5X5 cm^2 nominal area that was kept constant throughout the experiment. For data reproducibility, gouge layers were weighted after sample preparation. This procedure guaranteed similar porosity and a variability < 6% in the material density at the beginning of each test. During each test, σ_n is maintained constant at 5-10-20-30 MPa. For each of these normal stresses, experiments were conducted under both room-dry and wet conditions. Saturation was accomplished by placing the sample assembly in an impermeable plastic membrane filled with deionized water at the beginning of the tests.

To study the frictional properties of bare rock surfaces, experiments were designed in unconfined single-direct shear configuration, in which two blocks were juxtaposed to simulate a fault surface (Figure 1c). In this experimental geometry, the sliding area of 16 cm^2 was also kept constant during the test. Due to limited tensile strength of the unconfined basalt blocks in single-direct shear configuration, tests on bare rock surfaces were conducted up to 10 MPa normal stress.

The experimental procedure is common for both the configurations and consists in initially applying a normal stress of 1 MPa and let the sample compact. For wet experiments, samples were allowed to saturate for 30-40 min with deionized water. Subsequently, normal stress was increased stepwise to the target values and the sample compaction monitored, until the achievement of a steady-state value of horizontal shortening, usually reached after 30-40 min. At this point the vertical ram was advanced at a constant displacement rate of 10 µm/s to apply shear stress and induce shear deformation. We waited until a steady-state frictional strength was achieved, which for gouges requires a displacement of 6-7 mm and for bare surfaces 3 mm. This procedure was meant to develop steady-state shear fabric (e.g., *Haines et al.*, 2013) within the gouge layer, and to produce a relatively uniform surface roughness for bare surface experiments. The coefficient of stable sliding friction (μ_{ss}) at steady state was then computed as the ratio between the vertical force and the horizontal force applied by their respective rams, and assuming no cohesion (Table 1). In double-direct shear configuration, the vertical load was halved to average the friction coefficient within the two gouge layers.

Following the achievement of steady-state friction, two distinct types of tests were performed: velocity stepping tests are designed to investigate the velocity dependence of friction, thus the frictional constitutive behavior to infer fault slip stability, and slide-hold-slide (SHS) tests to measure time-dependent frictional restrengthening (Figure 1a; Table 1).

During velocity stepping tests, we imposed a series of computer-controlled velocity step increases in the following sequence, 0.1 – 0.3 – 1 – 3 - 10 – 30 – 100 – 300 µm s^{-1} with a constant displacement of 500 µm at each step. Each velocity step consisted in a quasi-instantaneous step increase in sliding velocity from V_0 to V and the new sliding velocity was kept constant until a new steady-state condition was attained (Figure 1d). To investigate the velocity dependence of friction, we modelled the collected data from each velocity step following the Dieterich's time-dependent formulation of the rate-and-state friction constitutive law

(*Dieterich*, 1979; *Marone*, 1998b), coupled with the slip evolution law proposed by *Ruina* (1983) as a description of the state evolution:

$$\mu = \mu_0 + a \ln \frac{V}{V_0} + b_1 \ln \frac{V_0 \theta_1}{D_{c1}} + b_2 \ln \frac{V_0 \theta_2}{D_{c2}} \quad \text{Eq. (1)}$$

$$\frac{d\theta}{dt} = -\frac{V \theta_i}{D_{ci}} \ln\left(\frac{V\theta_i}{D_{ci}}\right), \text{ i =1,2} \quad \text{Ruina's "slip" law} \quad \text{Eq. (2)}$$

where μ_0 represents the reference steady-state friction at the initial slip velocity V_0, a, b_1 *and* b_2 are empirically derived constants (dimensionless) termed direct and evolution effect, respectively, θ_1 *and* θ_2 are the state variable with units of time, D_{c1} *and* D_{c2} are the critical slip distances over which the state variables evolve to a new steady-state value following the velocity step (e.g., *Marone*, 1998b).

To model our data, we simultaneously solved Eq. (1) and (2) using a fifth order Runge Kutta numerical integration technique, with the time derivative of a one-dimensional elastic system as a constraint (Eq. (3)), which accounts for the finite stiffness of the testing apparatus and its elastic interaction with the frictional surface/gouge layers:

$$\frac{d\mu}{dt} = k (V_{lp} - V) \quad \text{Eq. (3)}$$

where V_{lp} is the load point velocity and k is the elastic loading stiffness of our experimental apparatus and the experimental fault, normalized by the normal stress (given in units of coefficient of friction per displacement). We then determined the constitutive parameters a, b, and Dc as in Figure 1e, by fitting our data from velocity step tests using an inverse modelling technique (e.g., *Blanpied et al.*, 1998a; *Reinen and Weeks*, 1993; *Saffer and Marone*, 2003). This technique also includes removing the slip-dependent linear trends in friction that accompany the velocity steps. In most cases, one state variable is sufficient to fit the experimental data; in such cases, the last term of Eq. (1) can be deleted by setting b_2 and θ_2 as null, so that $b = b_1$ and $Dc = Dc_1$. However, in some relatively low slip velocity steps ($V \leq 30$ μm/s), bare surfaces data are best described using the two state variables, where $D_c = D_{c1} + D_{c2}$ and $b = b_1 + b_2$.

We quantified the friction velocity dependence under steady-state sliding conditions through the friction rate parameter (a-b), defined as:

$$(a\text{-}b) = \Delta\mu_{ss} / \ln(V/V_0) \quad \text{Eq. (4)}$$

where $\Delta\mu_{ss}$ is the change in steady-state friction upon a step change in slip velocity from V_0 to V.
In the rate-and-state friction context, positive values of *(a-b)* define velocity strengthening behavior, that is associated with stable sliding, whereas negative values of *(a-b)*, termed velocity weakening behavior, are a requirement for the nucleation of unstable slip (e.g., *Marone*, 1998b; *Scholz*, 2002).

Time dependent frictional strength (i.e., frictional healing) was studied with slide-hold-slide (SHS) sequences that consist in alternating shearing at constant displacement rate of 10 μm/s with periods where the

fault is held under quasi-stationary contact ($V = 0$). We employed hold times (t_h) of 30, 100, 300, 1000, 3000 s with 500 μm displacement at 10 μm s^{-1} after each hold (Figure 1f).

The amount of frictional healing (Δμ) of both gouge layers and bare surfaces was determined for each hold time as the difference between peak friction measured upon re-shear and the steady-state friction value measured just before the hold, (e.g., *Frye and Marone*, 2002; *Marone*, 1998a; *Richardson and Marone*, 1999), (Figure 1g). By varying the hold time (t_h), we then determined the frictional healing rate (ß) for all the materials as:

$$ß = \Delta\mu/\log_{10}(t_h) \qquad \text{Eq. (5)}$$

The parameter ß provides an estimate of the rate of recovery of frictional strength.

2.2 Rotary-shear experiments

Friction experiments were also performed with the rotary-shear apparatus SHIVA (Slow to HIgh Velocity Apparatus), installed at the INGV in Rome (Italy). These tests were designed to interrogate the frictional strength at large displacement values that could not be reached with the biaxial deformation apparatus BRAVA (Figure 2).

SHIVA uses two brushless motors (maximum power 300 kW) in a rotary-shear configuration that supply the torque (i.e., shear stress) and the angular rotation, at nominally infinite slip. Normal load is applied to the experimental fault via an air actuator acting through a lever to amplify the resulting normal load (2t amplified to 5t). Mechanical data including axial load, torque, axial shortening, and angular rotation were acquired at a frequency of 12.5 Hz. Further details on the experimental apparatus, the control and acquisition system can be found in *Di Toro et al.* (2010) and *Niemeijer et al.* (2011). The experiments were performed on hollowed rock cylinders of basalts 50/30 mm external/internal diameter. Specimens were ground flat and parallel using a surface grinder, jacketed in aluminum ring, and embedded in epoxy, following the protocol described in *Nielsen et al.* (2012). This procedure ensures misalignment smaller than 100 μm when the samples are juxtaposed and mounted on SHIVA to simulate rock-on-rock frictional sliding. To obtain the same starting average roughness as in the slabs installed in BRAVA, basalt cylinders were subsequently roughened with #80 grit silicon carbide powders as in the direct-shear tests.

All the experiments were conducted at nominally 4 - 8 - 12 MPa normal stress and specified displacement rate of 10 μm/s, under both room-dry and wet conditions. To perform experiments at wet conditions, SHIVA was equipped with a pressure vessel that allowed sample saturation (*Violay et al.*, 2013, 2014). The chamber of the pressure vessel was filled with deionized water via an ISCO Teledyne Pump, by injecting fluid at atmospheric pressure. In order to prevent fluid overpressure throughout the tests, all the experiments were carried out under drained conditions, and the fluid pressure monitored via the fluid pressure sensors located at about 5 mm from the fault zone and internally the ISCO pump.

Furthermore, to further reduce the possible sample misalignment along the frictional interface, at the beginning of each experiment, the fault was slid for 2 mm at room-dry conditions ("shear run-in" phase), and the normal and shear load subsequently removed. In wet experiments, fault saturation followed the "run-in" phase. After reapplication of normal load, we reiterated sliding episodes of length 2 mm at 10 μm/s, followed by 2 min of hold time (displacement rate = 0), up to 8 mm slip. Then, the fault was slid steadily at 10 μm/s until the achievement of 48 mm displacement. Finally, we performed a second slide-hold-slide sequence (Figure 2) reaching a cumulative slip of 56 mm. These cycles were intended to monitor the fault strength evolution within small cumulative slip intervals, but since a very small increase in frictional strength within each 2 mm sliding episode is observed, we report only the measurements at 4- and 56-mm net displacements (Table 2).

2.3 Dilatancy measurements

Dilation of granular layers due to velocity steps have been widely documented: gouge layers generally dilate in response to a velocity step increase, whereas overall compaction is expected to accompany step decreases in slip velocity (e.g., *Marone et al.*, 1990). Specifically, dilation magnitude represents a good proxy for the volumetric strain changes, hence the thickness of the shear band accommodating strain (*Marone and Kilgore*, 1993) and ultimately, the degree of strain localization: the higher the strain localization, the lower is the corresponding dilation velocity dependence.

To determine the gouge layer evolution upon step changes in loading velocity, we measured variation in layer thickness at constant normal stress by monitoring the horizontal LVDT displacement, in accordance with the approach outlined in *Samuelson et al.* (2009) and *Scuderi et al.* (2013) (see also *Mair and Marone*, 1999; *Marone et al.*, 1990; *Scuderi et al.*, 2017). As gouge layers thin quasi-continuously with displacement due to simple shear (e.g., *Scott et al.*, 1994), we removed monotonic long-term trends in layer thickness prior to assessing dilation related to velocity perturbations (Figure 3a). We therefore define ΔH as the steady-state layer dilation in response to the velocity steps (*Marone and Kilgore*, 1993), averaged over the slip accumulated following the step changes in velocity (Figure 3b).

The same method has been applied during the slide-hold-slide tests (Figure 4a), in which the hold phase is accompanied by gouge layer compaction Δh_c, while steady-state dilation ΔH occurs as load point resumes (Figure 4b,c) (see *Frye and Marone*, 2002; *Karner and Marone*, 2001 for further details). Pore volume changes paired with load point perturbations during SHS tests may provide insights on the microphysical processes responsible for the frictional healing in simulated gouge layers. Such changes were monitored at different environmental conditions (i.e., room-dry and wet conditions) to shed light on the possible contribution of compaction on the frictional restrengthening between slip events in basalts.

2.4 Microscopy investigations

We collected photo-mosaics of the whole thin section length and thickness with the DeltaPix M12Z optical microscope, and micrographs of the thin section details at higher magnification using a JEOL JSM-6500 F thermal field emission scanning electron microscope (FE-SEM). All the micrographs taken with the FE-SEM were back-scattered electron images. Both microscopes are located at INGV – Rome (Italy).

3.RESULTS

3.1 Frictional strength

After the initially nearly linear-elastic loading phase, the friction vs. slip curve reaches a steady-state value (τ_{ss}) with increasing displacement, at the end of the run-in phase (Figure 1a, Figure 2). The steady-state shear strength scales linearly with the applied normal stress irrespective of the tested simulated faults, environmental conditions, and sample configurations, and can be fitted with a linear regression accordingly to the Amontons' law and with the associated coefficient of stable sliding friction, μ_{ss} at steady state.

Frictional sliding data reported in Figure 5 range from μ_{ss} = 0.59 to 0.78. Collectively, data agree well with Byerlee's rule for friction (*Byerlee*, 1978). Differences in sliding friction between tests performed under room-dry and wet conditions, if any, are contained in the error.

Notably, within the small friction range observed, rock-on-rock experiments revealed systematic discrepancies between the average frictional sliding measured at low displacements for bare surfaces deformed on BRAVA (μ_{ss} = 0.76) and hollow cylinders mounted on SHIVA (μ_{ss} = 0.63). The latter exhibited a very small positive rate of displacement hardening with cumulative displacement, with friction increasing from about 0.6 upon initial sliding to ~ 0.7 after 56 mm slip. We also report a slightly higher friction coefficient in bare surfaces than in simulated gouge (average μ_{ss} = 0.62), *ceteris paribus*.

3.2 Frictional stability

The friction rate parameter *(a-b)* for velocity steps of experiments conducted on both fault gouge and bare surfaces is reported in Figures 6 and 7, respectively. For experiments involving simulated fault gouge, the examination of the friction rate parameter *(a-b)* reveals a dependence on the normal stress and sliding velocity for both dry and wet samples. Our results show that for normal stress larger than 5 MPa, the frictional behavior is progressively velocity weakening with the increase of sliding velocity (Figure 6a, Table 3). Notably, at σ_n = 30 MPa simulated fault gouge transitions to slightly velocity weakening/velocity neutral behavior, with room-dry powders exhibiting a lower weakening rate when compared to their wet equivalents. At the lowest normal stress, i.e., σ_n = 5 MPa, this tendency changes to a velocity strengthening behavior at $V > 30$ μm/s, markedly under wet conditions (Figure 6a).

We further investigate the frictional behavior of simulated fault gouge by exploring the evolution of the individual friction rate parameters *a* and *b*. Overall, the experiments on simulated fault gouge show no discernable increase in direct effect *a* with increasing velocities. The only exception concerns the tests performed at σ_n = 30 MPa, where we observed progressively larger direct effect at the highest velocities, especially for the tests involving DI H_2O (Figure 6b). We find that *(a-b)* is mostly influenced by the evolution of the friction velocity parameter *b*. In fact, at σ_n = 5 MPa *b* shows a negative trend with increasing sliding velocities (Figure 6c), yielding b < *a* and thus a velocity strengthening behavior. Whereas, from 10 to

30 MPa, *b* becomes progressively larger than *a* as we approached higher velocities (Figure 6b,c), justifying the transition from velocity strengthening/neutral to velocity weakening behavior.

Experiments on bare rock surfaces revealed a positive dependence of *(a-b)* on shear velocity *V*. We find a transition from velocity weakening at $V \leq 3$ μm to velocity strengthening behavior at the highest velocities in particular in the case of dry surfaces. This evolution is still persistent on wet samples but less pronounced. (Figure 7, Table 3). Moreover, we note a systematic negative slip dependence of friction for all the velocity stepping tests involving shear along bare surfaces (Figure 1a).

3.3 Frictional healing

In Figure 8a are displayed the healing values at different normal stresses against hold time. Frictional healing data Δμ show positive values over the entire sample suite. In detail, data involving shearing of bare rock surfaces show the largest healing rates, in the range ß = 0.0211 – 0.0265. Experiments performed with simulated fault gouge systematically exhibit lower values of healing rate than the bare surfaces equivalents, with ß from 0.0051 to 0.0128.

We also found that frictional healing for synthetic gouge evolved differently depending upon the environmental conditions: simulated fault gouges in the presence of DI water have higher frictional strengthening rates (ß = 0.0091 to 0.0128) compared to room-dry samples (ß = 0.0051 to 0.0063) (Table 3). In contrast, such divergence was not evident in bare rock surfaces friction experiments. Furthermore, none of the experimental faults we studied showed a clear dependence of ß on the normal stress.

3.4 Volumetric deformation during velocity steps and slide-hold-slides

In all our tested conditions, we notice that: *(a)* each velocity upstep corresponds to a transient and steady-state increase in gouge layer dilation and *(b)* volumetric strain changes occur over the same distance as the slip required for reaching a new steady-state friction level upon the velocity upsteps, and therefore are significant for the stability of sliding (e.g., *Rice and Ruina,* 1983) (Figure 3b). Steady-state dilation values ΔH were plotted against normal stress (Figure 9).

Overall, the experiments show an increase in ΔH with increasing sliding velocity in the range of $0.2 < \Delta H < 1.4$ μm, but smaller dilation values towards larger normal stresses. Under wet conditions, samples sheared at $\sigma_n = 5$ MPa exhibit higher ΔH when compared to their room-dry equivalents (Figure 9). Due to the higher noise characterizing the H-LVDT data for initially bare surfaces, we could not investigate the dilation during such velocity steps.

Similarly, only in a few cases dilation ΔH and compaction Δh_c measurements were possible following SHS tests. In particular, analysis of volumetric changes during such tests, indicate that positive

healing rates are accompanied by compaction Δh_c during hold and dilation ΔH at slip initiation (Figure 8). The Δh_c and ΔH values are generally higher for powders relative to bare surfaces (Figure 8b,c). We find that dilation ΔH at slip initiation in simulated gouge increases log-linearly with hold time, with the largest magnitudes found at the lowest normal stresses under wet conditions (Figure 8b). Conversely, the compaction Δh_c data display a bimodal trend depending on the environmental conditions: SHS compaction increases linearly with log hold time in gouge layers sheared under wet conditions, which is consistently higher in comparison to their room-dry analogues, for the entire range of conditions investigated (Figure 8c).

3.5 Microstructural observations

3.5.1 Simulated fault gouge

We carried out microstructural analysis at the optical and scanning electron microscopes on our deformed gouge layers which had been impregnated with low viscosity epoxy resin after unloading. Our main observations point to a progressive microstructural reorganization with increasing normal stresses, under both room-dry and wet conditions. The entire compilation of optical micrographs is displayed in Figure S5, Suppl. Mat.

3.5.1.1 Simulated gouge: low normal stresses microstructures

Under wet conditions, at low normal stress (σ_n < 10 MPa), we observed the development of incipient shear bands along Riedel R1 and B orientations (*Logan*, 1979). Proto-B shears are continuous, located at both sides of the fault zone. Conversely, proto-R1 are discontinuous, they start from the boundaries of the gouge layers and subsequently curve at low angle (~ 15°) with the direction of shear (Figure 10a).

Both shear bands are characterized by a thickness of ~ 50-70 μm (Figure 10b,c), enriched in fine-grained material that surrounds larger angular clasts isotropically-oriented (Figure 10c). The shear bands include grains with comparable dimension to that of the starting material (Figure S4, Suppl. Mat.). Under dry conditions, we do not observe the development of incipient R1 and B shear bands.

3.5.1.2 Simulated gouge: higher normal stress microstructures

Observations under the optical and scanning electron microscope reveal shear bands R1 and B affected by significant grain-size reduction (Figure 11). This testifies that at higher normal stresses (i.e., $\sigma_n \geq 10$ MPa), shear deformation was predominantly localized along well-developed shear bands B and R1, whilst particles essentially retained their original size elsewhere in the gouge.

Comparisons with the microstructures observed at 5 MPa indicate a progressive sharpening and thickening of B and R1 shears with increasing normal stress (from 70 to 200 um thickness with σ_n in the range 5-30 MPa). Both B and R1 shear bands are the loci of cataclastic processes with extensive grain size reduction (GSR in Figure 11b; see also e.g., *Logan*, 1979; *Logan and Rauenzahn*, 1987; *Logan et al.*, 1992). Shear bands B and R1 are typically separated by relic pockets of relatively undeformed material and consist of sub-angular larger clasts, with grain size comparable with the starting material (~ 20 -70 µm), sustained by a fine-grained matrix (Figure 11c). Larger clasts located within the shear zones and at the shear bands interfaces are characterized by limited chipping and fracturing (e.g., *Billi*, 2010), whereas fine-grained material consists of angular grains with size << 10 µm, derived from localized cataclasis and also from the starting material due to the plausible redistribution of finer undeformed basalt grains along shear zones. Both larger and fine grains are randomly oriented within the bulk gouge layer.

3.5.2 Bare rock surfaces

In sliding experiments executed with bare rock surfaces, samples exhibited similar macroscopic deformation structures despite differences in geometry of the specimens and in the deformation apparatuses.

The slipping zones that are produced at the end of each experiment consist of lineated principal slip surfaces, characterized by a few microns-thick cohesive gouge with mechanical wear streaks along the entire slipping surface, elongated in the slip direction (Figure 12a and b). The gouge overlies the slip surfaces and covers the grooves ploughed into the basalt surfaces during shearing of the surface asperities. As anticipated, slip surfaces subjected to higher normal stresses produce more wear material with progressive slip (Figure S6, e.g., *Badt et al.*, 2016; *Tesei et al.*, 2017).

Furthermore, cylinders deformed on SHIVA at room-dry conditions also preserved tool marks consisting of high relief gouge patches displaced by slip-perpendicular steps (Figure 12a). This feature was not observed during wet experiments, since most of the gouge layer was flushed away with water during the sample recovery, as previously pointed out e.g., by *Violay et al.* (2013) and *Giacomel et al.* (2018).

4.DISCUSSION

4.1: The role of localization vs. delocalization in basalt fault slip behavior

We merge our mechanical data with microstructural analysis to gain better insights on the physical processes at the origin of the frictional properties of basalt faults.

As anticipated, fault strength in our tests is in the range of the Byerlee's rule for friction and varies only slightly among tests employing different experimental configurations and sample geometries, given the relative friction data scatter expected at low normal stresses for solid silicate-bearing rocks (*Byerlee*, 1978). This evidence testifies that our data are not particularly affected by artifacts resulting from the experimental design. Minor discrepancies in sliding friction coefficient deriving from the different sample geometries we employed may be due to *(i)* local stress heterogeneities along bare rock surfaces, which could arise from the 0.1 mm tolerance of the sample grinder as well as the starting roughness, *(ii)* possible different textural evolution characterizing shear within gouge and between bare rock surfaces, and (*iii*) the different method employed in direct shear and rotary shear configurations to calculate the shear stress acting along the frictional interface (see *Shimamoto and Tsutsumi, 1994* for details). Furthermore, the small displacement hardening observed in rotary shear tests reflects the accumulation of a ~ 50 μm thick gouge layer coating on the sliding bare surfaces after 56 mm slip, in good agreement with findings of *Marone and Cox* (1994) and *Mitchell et al.* (2015) on bare surfaces of gabbros at 5 MPa normal stress. The elevated healing rates (ß) regardless of the simulated fault type employed in our tests, coupled with the high frictional strength are typical hallmarks of faults with frictionally strong mineral phases such as the primary phases constituting basalts i.e., olivine, pyroxene, and plagioclase. Within this framework, the highest healing rates related to basalt bare surfaces can be interpreted in terms of asperity interaction and specifically, by invoking a larger contact junction size for bare surfaces with respect to simulated gouge. The positive correlation between higher friction restrengthening and compaction rates in wet compared to room-dry gouge samples, attests that compaction Δh_c during the hold periods represents a key fraction of the frictional healing in (unaltered) basalt fault gouge, which is aided by the presence of water (Figure 8a,c). However, we cannot rule out that slip-dependent processes also participated in fault restrengthening during creep relaxation, nor a possible contribution of water-assisted time-dependent strengthening of grain contacts (e.g., *Frye and Marone*, 2002).

For the velocity dependence of friction, our results illustrate heterogeneous frictional stability behavior according to the different configurations, represented by bare rock surfaces or simulated fault gouge, and the normal stress at which faults are subjected. The frictional behavior of bare surfaces and simulated fault gouge is the opposite with increasing velocity and displacement.

Regarding powdered gouge, we find that the measurements of friction rate dependence, dilation, and microstructural observations are interrelated. In wet samples deformed at 5 MPa normal stress, *(i)* the small friction rate parameter *b* throughout the velocity stepping sequences (Figure 6c), associated with *(ii)* the limited grain size reduction characterizing proto-R1 and proto-B shears (Figure 10) and *(iii)* the large gouge

layer dilation at high velocities (Figure 9), testify that deformation is essentially distributed within the bulk volume of the simulated fault gouge, and explains the recognized rate strengthening behavior as we approached higher slip velocities (Figure 6a). Therefore, we posit that due to the low applied normal stress, it is likely that the incipient shear bands mostly derive from the accumulation of fine grains from the regions of the starting material exhibiting small particle sizes. As a consequence, we infer that much of the deformation was accommodated via frictional sliding at the grain contacts, rotation, and translation during shearing, rather than grain comminution processes (e.g., *Biegel et al.*, 1989; *Engelder*, 1974). The same conclusion can be drawn in dry powders characterized by the lack of proto-R1 and proto-B shears, suggesting that the whole bulk gouge volume was participating in fault shearing (Figure S5). However, the more pronounced velocity strengthening behavior in wet experiments at the highest slip velocities (Figure 6a), is probably due to the more significant dilation effect compared to their room-dry equivalents (Figure 9), which entails a higher excess in work done against the normal stress (*Marone et al.*, 1990) and thus a higher frictional resistance upon velocity upsteps.

On the contrary, at $\sigma_n \geq 10$ MPa, the progressively larger b with slip velocity (Figure 6c) correlates with the observed strain localization along continuous R1 and B shears bands accompanied by cataclasis and grain size reduction (Figure 11), resulting in the recorded velocity weakening behavior, as previously reported by laboratory observations on simulated gouge (e.g., *Mair and Marone*, 1999). The enhanced strain localization at $\sigma_n \geq 10$ MPa is also corroborated by the overall lower dilation values recorded at progressively higher normal stresses during the velocity steps (Figure 9), as well as upon re-shearing during the SHS sequences (Figure 8b). The velocity weakening behavior, induced by shear localization, coupled with the high healing rates and high shear strength, render fault zones characterized by basalt gouge good candidates to host the nucleation of seismic events.

In marked contrast, the positive evolution of the friction rate parameter (*a-b)* with increasing slip velocity in bare surfaces sheared at σ_n = 5 to 10 MPa (Figure 7), results in a transition to slightly or strong rate strengthening behavior for wet and room-dry conditions, respectively. A possible explanation for the switch to rate-strengthening behavior could involve shear delocalization that may have occurred due to frictional wear production and played a key role in strengthening the bare surfaces upon velocity steps. It is indeed well documented that gouge accumulation during shear of initially bare surfaces tends to stabilize slip, especially at low applied normal stresses (*Byerlee*, 1967; *Byerlee and Summers*, 1976; *Scholz et al.*, 1972; *Engelder et al.*, 1975; *Wong et al.*, 1992). In addition, the experimental work documented in *Marone et al.* (1990) and *Marone* (1998b) highlights the strict relation between strain delocalization following the presence of a gouge layer during slip along bare rock surfaces and the increase in the friction rate parameter *(a-b)*. This effect is further magnified with increasing the initial surface roughness. Recent published studies by *Ikari et al.* (2020) at 25 MPa effective normal stress, further corroborate the pivotal role played by shear dilation during the velocity steps, causing the switch to velocity strengthening friction even when slip nucleates along altered (clay-rich) basalt rock-on-rock contacts (Figure 7). In the light of these observations,

comparisons between friction stability data covering small net displacements (≤ 12 mm) on *a)* (unaltered) gabbro bare surfaces from *Marone and Cox*, (1994) at 5 MPa normal stress, *b)* (unaltered) basalt surfaces from our tests, and *c)* (altered) basalt surfaces from *Ikari et al.* (2020) (Figure 7), point to an inherent tendency for unstable sliding at low slip velocities in frictionally strong bare surfaces of basalts and gabbros, which is overcome by a strengthening effect at higher velocities due to changes in dilatancy rates.

To summarize, we postulate that (unaltered) simulated fault gouge and rough bare surfaces represent two basalt microstructural end-members, whose contrasting evolution of the rate and state constitutive parameter (*a-b)* with increasing sliding velocity and slip possibly results from two opposite mechanical processes operating during frictional sliding: on one hand, shear within simulated fault gouge is characterized by cataclasis with grain size reduction and localization that facilitates the transition to velocity neutral/weakening behavior; on the other hand, gouge development during slip along bare surfaces likely involves shear delocalization that entails the evolution towards velocity strengthening behavior. However, we envisage that dilatancy-strengthening is probably a small net displacement process, because, as we observed from our tests at large accumulated slip, the bare surfaces are likely to be greatly affected by production of gouge during shearing (Figure 12a), in particular with increasing normal stresses (Figure S6). We thus posit that at large displacements, once gouge layer becomes thick enough with respect to the bare surface roughness, rock surfaces separated by the gouge layer would start to localize deformation within the gouge, that would lead samples to become progressively velocity weakening and potentially unstable (Figure 6a).

4.2: Implications for the slip behavior of shallow faults in volcano-tectonic settings and basalt-hosted geo-energy sites

In our laboratory friction experiments, we investigated an effective normal stress interval of 5-30 MPa, which corresponds to an *in-situ* depth up to ~ 2-3 km, depending on hydrostatic or supra-hydrostatic fluid pressure levels. At these inferred depths, wet conditions are expected to represent more realistic conditions of shearing rather than room-dry tests. It should be emphasized that the experimental protocol enables us to investigate the friction stability and healing rates at low strains (γ~4) and displacements, implying that our tests mimic only the early stages of microstructural evolution that accompanies slip localization within unaltered basalt fault gouge or competent rock. Therefore, our data provide mechanical connections with unaltered basalt gouge-rich shear zones and incipient fault zones in the presence of pervasive jointed networks, such as those potentially located in CarbFix-like sites or active shallow volcano-tectonic settings. In these geological environments the documented combination of high-strength for unaltered basalt fault gouge, with prevalent velocity weakening behavior and important healing rates, define potentially unstable zones that would explain some of the slip instabilities documented in active volcano-tectonic settings such as along the shallow flanks and edifices of the Hawaiian (*Denlinger and Morgan*, 2014; *Klein et al.*, 1987; *Lockwood et al.*, 1987) and Etnean (*Alparone et al.*, 2013; *Azzaro et al.*, 2017) volcanoes. On the contrary, fault maturity within basalt shear zones and associated fluid assisted reaction softening promote the development of interconnected clay networks that would favor the transition to a predominant velocity strengthening friction, thus a tendency for stable sliding behavior (Figure 6a; *Ikari et al.*, 2011, 2020).

The documented switch from velocity weakening to strengthening of bare surfaces with increasing sliding velocity indicates that slip initiation in rough jointed surfaces may be possible at slow sliding velocity ($V \leq 10$ μm/s), yet unstable slip would be suppressed at higher rates, resulting either into stable sliding or limited coseismic slip rates, stress drop and cumulated slip (e.g., *Blanpied et al.*, 1998b; *Weeks*, 1993). In this second scenario, the superposition of the negative slip dependence of friction following the velocity steps (Figure 1a) may counteract the slightly velocity strengthening/neutral behavior at the highest slip velocities (Figure 7), and possibly result in a net weakening that would favor slip acceleration even at higher slip rates than predicted from our rate-and-state friction analysis (*Ikari et al.*, 2013; *Ito and Ikari*, 2015). This observation, coupled with the significant propensity of bare surfaces to regain strength following the slip events (Figure 8a), suggests the possibility to develop potential unstable faults from incipient basalt jointed networks with important implications for the long-term integrity and stability of basalt-hosted geo-energy sites, including the CO_2 repositories.

5.CONCLUSIONS

We carried out a series of laboratory friction experiments intended to explore the role of experimental fault microstructure, defined by simulated gouge and rough bare rock surfaces, on the frictional properties and constitutive parameters of unaltered basalt-built faults. Samples were deformed under room-dry and wet conditions in a direct- and a rotary-shear configuration, at normal stresses up to 30 MPa at ambient temperature, which are deemed to represent the conditions for fault slip in some areas such as those potentially suitable for in-situ geological carbon storage and active volcano-tectonic settings.

Our results indicate that: *(1)* the elevated friction coefficient (μ = 0.59- 0.78) and high healing rates (ß = 0.0055 – 0.0265) render basalt faults frictionally strong and able to rapidly regain the shear strength necessary for repeated fault reactivation throughout the geological fault history; *(2)* shear along bare rock surfaces and within simulated gouge led to opposite frictional stability behavior in the velocity range investigated (V = 0.1 – 300 µm/s): while powdered gouge switch to velocity weakening behavior with increasing slip velocity and displacement, bare surfaces transition to velocity strengthening behavior. Consequently, *(3)* the strong correlation at increasing normal stress between velocity weakening behavior and shear localization along B and R1 shear bands with grain size reduction, coupled with the high healing rates and high shear strength, render fault zones characterized by basalt gouge good candidates to potentially host seismic nucleation and rupture propagation, *(4)* the observed velocity strengthening behavior accompanied by gouge production during shearing would render initially rough bare surfaces less prone to unstable slip.

Overall, we envisage from our tests that a thorough knowledge of the complexity of fault microstructure would be of paramount importance to mitigate the seismic risk associated to volcano-tectonic regions dominated by basalts and before embarking in industrial scale geo-energy projects, where large volumes of fluid are anticipated to be injected into such formations. Nonetheless, further research aimed at investigating how textural and mineralogical maturity, temperature, and pore fluid pressure may influence the frictional strength, stability and healing properties of basalt-built faults, would be warranted to extend the laboratory-based seismic risk assessment to a broader range of targets-bearing basaltic rocks.

AUTHOR CONTRIBUTIONS:

PG wrote the first version of the manuscript. CC, PG, ES, MMS, GDT conceived the idea of the experiments. PG performed the petrophysical and microstructural analyses. RR, MMS, PG, ES performed the experiments. All the authors analyzed the mechanical and microstructural data and contributed to the final version of the manuscript.

ACKNOWLEDGEMENTS:

This work has benefited from the European Research Council project 614705 NOFEAR and Progetti di Ateneo La Sapienza Collettini 2018 grants. We are grateful to F.lli LIZZIO S.r.l. for providing Etnean basalt samples. We acknowledge D. "Mimmo" Mannetta, L. Tauro, and E. Masiero for thin section preparations and sample saw-cut, F. Zorzi for XRF and XRPD analyses, M. Nazzari for providing assistance with the SEM, and S. Mollo and E. Del Bello for technical support for the use of the He-pycnometer and the Separation Analyzer LUMiReader. We thank C. Marone for the XLook program for obtaining RSF parameters. CWA Harbord and S. Aretusini are acknowledged for technical support in the HP-HT laboratory and during SHIVA experiments. Telemaco Tesei is thanked for insightful discussion regarding this study. Carolina Giorgetti is thanked for her precious and constructive comments that helped to improve the quality of this study.

Dataset related to this article can be accessed at https://dataservices.gfz-potsdam.de/panmetaworks/review/c3849f80a7920f7735354d90e66[illegible]b553c36e20222a07f8763477b5870ce9657c/ (*Giacomel et al., 2021*) via the open source GFZ Data Services.

CREDIT AUTHOR STATEMENT

PG wrote the first version of the manuscript. CC, PG, ES, MMS, GDT conceived the idea of the experiments. PG performed the petrophysical and microstructural analyses. RR, MMS, PG, ES performed the experiments. All the authors analyzed the mechanical and microstructural data and contributed to the final version of the manuscript.

Declaration of interests

The authors declare that they have no known competing financial interests or personal relationships that could have appeared to influence the work reported in this paper.

REFERENCES

Aki, K., & Ferrazzini, V. (2001). Comparison of Mount Etna, Kilauea, and Piton de la Fournaise by a quantitative modeling of their eruption histories. *Journal of Geophysical Research: Solid Earth*, *106*(B3), 4091-4102.

Alfredsson, H. A., E. H. Oelkers, B. S. Hardarsson, H. Franzson, E. Gunnlaugsson, and S. R. Gislason (2013), The geology and water chemistry of the Hellisheidi, SW-Iceland carbon storage site, *International Journal of Greenhouse Gas Control*, *12*, 399-418, doi:10.1016/j.ijggc.2012.11.019.

Alparone, S., Cocina, O., Gambino, S., Mostaccio, A., Spampinato, S., Tuvè, T., & Ursino, A. (2013). Seismological features of the Pernicana–Provenzana Fault System (Mt. Etna, Italy) and implications for the dynamics of northeastern flank of the volcano. *Journal of volcanology and geothermal research*, *251*, 16-26.

Azzaro, R., G. Barberi, S. D'Amico, B. Pace, L. Peruzza, and T. Tuvè (2017), When probabilistic seismic hazard climbs volcanoes: the Mt. Etna case, Italy – Part 1: Model components for sources parameterization, *Nat. Hazards Earth Syst. Sci.*, *17*(11), 1981-1998, doi:10.5194/nhess-17-1981-2017.

Azzaro, R., D'Amico, S., Peruzza, L., & Tuvè, T. (2013). Probabilistic seismic hazard at Mt. Etna (Italy): the contribution of local fault activity in mid-term assessment. *Journal of volcanology and geothermal research*, *251*, 158-169.

Badt, N., Y. H. Hatzor, R. Toussaint, and A. Sagy (2016), Geometrical evolution of interlocked rough slip surfaces: The role of normal stress, *Earth and Planetary Science Letters*, *443*, 153-161, doi:10.1016/j.epsl.2016.03.026.

Ben-Zion, Y. (2001), Dynamic ruptures in recent models of earthquake faults, *Journal of the Mechanics and Physics of Solids*, *49*(9), 2209-2244, doi:https://doi.org/10.1016/S0022-5096(01)00036-9.

Billi, A. (2010), Microtectonics of low-P low-T carbonate fault rocks, *Journal of Structural Geology*, *32*(9), 1392-1402, doi:10.1016/j.jsg.2009.05.007.

Biegel, R. L., C. G. Sammis, and J. H. Dieterich (1989), The frictional properties of a simulated gouge having a fractal particle distribution, *Journal of Structural Geology*, *11*(7), 827-846, doi: https://doi.org/10.1016/0191-8141(89)90101-6.

Blanpied, M. L., Marone, C. J., Lockner, D. A., Byerlee, J. D., & King, D. P. (1998a). Quantitative measure of the variation in fault rheology due to fluid-rock interactions. *Journal of Geophysical Research: Solid Earth, 103(B5), 9691-9712*, doi:10.1029/98jb00162.

Blanpied, M. L., T. E. Tullis, and J. D. Weeks (1998b), Effects of slip, slip rate, and shear heating on the friction of granite, *Journal of Geophysical Research B: Solid Earth*, *103*(1), 489-511.

Boatwright, J., and M. Cocco (1996), Frictional constraints on crustal faulting, *Journal of Geophysical Research: Solid Earth*, *101*(B6), 13895-13909, doi:10.1029/96JB00405.

Brace, W. F., and J. D. Byerlee (1966), Stick-Slip as a Mechanism for Earthquakes. *Science*, *153*(3739), 990-992, doi:10.1126/science.153.3739.990.

Branca, S., M. Coltelli, and G. Groppelli (2011), Geological evolution of a complex basaltic stratovolcano: Mount Etna, Italy, *Italian Journal of Geosciences*, *130*(3), 306-317.

Byerlee, JD. (1967). Frictional characteristics of granite under high confining pressure. *J. Geophys. Res.* 72:3639–48.

Byerlee, J. (1978), Friction of rocks, *pure and applied geophysics*, *116*(4), 615-626, doi:10.1007/BF00876528.

Byerlee, J., & Summers, R. (1976, January). A note on the effect of fault gouge thickness on fault stability. In *International Journal of Rock Mechanics and Mining Sciences & Geomechanics Abstracts* (Vol. 13, No. 1, pp. 35-36). Pergamon.

Carpenter, B. M., M. M. Scuderi, C. Collettini, and C. Marone (2014), Frictional heterogeneities on carbonate-bearing normal faults: Insights from the Monte Maggio Fault, Italy. *Journal of Geophysical Research: Solid Earth*, *119*(12), 9062-9076, doi:10.1002/2014jb011337.

Cashman, K. V., Thornber, C. R., & Pallister, J. S. (2008). *From dome to dust: Shallow crystallization and fragmentation of conduit magma during the 2004-2006 dome extrusion of Mount St. Helens, Washington* (No. 1750-19, pp. 387-413). US Geological Survey.

Collettini, C., and R. H. Sibson (2001), Normal faults, normal friction?, *Geology*, *29*(10), 927-930, doi:10.1130/0091-7613(2001)029<0927:Nfnf>2.0.Co;2.

Collettini, C., G. Di Stefano, B. Carpenter, P. Scarlato, T. Tesei, S. Mollo, F. Trippetta, C. Marone, G. Romeo, and L. Chiaraluce (2014), A novel and versatile apparatus for brittle rock deformation, *International Journal of Rock Mechanics and Mining Sciences*, *66*, 114-123, doi:10.1016/j.ijrmms.2013.12.005.

Collettini, C., T. Tesei, M. Scuderi, B. Carpenter, and C. Viti (2019), Beyond Byerlee friction, weak faults and implications for slip behavior, *Earth and Planetary Science Letters*, *519*, doi:10.1016/j.epsl.2019.05.011.

Cox, S. J. D., Velocity dependent friction in a large direct shear experiment on gabbro. In *Deformation Mechanisms, Rheology, and Tectonics* (eds. Knipe, R. J. and Rutter, E.H.) (Geol. Soc. London 1990) Spec. Pub. *54*, pp. 63-70.

Denlinger, R. P., & Morgan, J. K. (2014). *Instability of Hawaiian volcanoes: Chapter 4 in Characteristics of Hawaiian volcanoes* (No. 1801-4, pp. 149-176). US Geological Survey.

Di Stefano, R., C. Chiarabba, L. Chiaraluce, M. Cocco, P. De Gori, D. Piccinini, and L. Valoroso (2011), Fault zone properties affecting the rupture evolution of the 2009 (Mw 6.1) L'Aquila earthquake (central Italy): Insights from seismic tomography, *Geophysical Research Letters*, *38*(10), doi:10.1029/2011GL047305.

Di Toro, G., Niemeijer, A., Tripoli, A., Nielsen, S., Di Felice, F., Scarlato, P., ... & Smith, S. (2010). From field geology to earthquake simulation: a new state-of-the-art tool to investigate rock friction during the seismic cycle (SHIVA). *Rendiconti Lincei*, *21*(1), 95-114, doi:10.1007/s12210-010-0097-x.

Dieterich, J. H. (1979), Modeling of rock friction: 1. Experimental results and constitutive equations, *Journal of Geophysical Research*, *84*(B5), doi:10.1029/JB084iB05p02161.

Engelder, J. T. (1974), Cataclasis and the generation of fault gouge, *Geological Society of America Bulletin*, *85*(10), 1515-1522.

Engelder JT, Logan JM, Handin J. 1975. The sliding characteristics of sandstone on quartz fault-gouge. *Pure Appl. Geophys.* 113:69–86

Frye, K. M., and C. Marone (2002), Effect of humidity on granular friction at room temperature, *Journal of Geophysical Research: Solid Earth*, *107*(B11), ETG 11-11-ETG 11-13, doi:10.1029/2001jb000654.

Garcia, M. O., & Davis, M. G. (2001). Submarine growth and internal structure of ocean island volcanoes based on submarine observations of Mauna Loa volcano, Hawaii. *Geology*, *29*(2), 163-166.

Giacomel, P., E. Spagnuolo, M. Nazzari, A. Marzoli, F. Passelegue, N. Youbi, and G. Di Toro (2018), Frictional Instabilities and Carbonation of Basalts Triggered by Injection of Pressurized H2 O- and CO2 -Rich Fluids, *Geophysical Research Letters*, doi:10.1029/2018gl078082

Giacomel, P.; Ruggieri, R.; Scuderi, M. M.; Spagnuolo, E.; Di Toro, G.; Collettini, C. (2020): Mechanical data of simulated basalt-built faults from rotary shear and direct shear experiments. GFZ Data Services. https://doi.org/DOI_when available

Gislason, S. R., D. Wolff-Boenisch, A. Stefansson, E. H. Oelkers, E. Gunnlaugsson, H. Sigurdardottir, B. Sigfusson, W. S. Broecker, J. M. Matter, and M. S. te (2010), Mineral sequestration of carbon dioxide in basalt: A pre-injection overview of the CarbFix project, *International Journal of Greenhouse Gas Control*, *4*(3), 537-545, doi:10.1016/j.ijggc.2009.11.013.

Goldberg, D. S., Kent, D. V., & Olsen, P. E. (2010). Potential on-shore and off-shore reservoirs for CO2 sequestration in Central Atlantic magmatic province basalts. *Proceedings of the National Academy of Sciences*, *107*(4), 1327-1332.

Haines, S. H., B. Kaproth, C. Marone, D. Saffer, and B. van der Pluijm (2013), Shear zones in clay-rich fault gouge: A laboratory study of fabric development and evolution, *Journal of Structural Geology*, *51*, 206-225, doi: https://doi.org/10.1016/j.jsg.2013.01.002

Hatton, C.G., Main, I.G., and Meredith, P.G., 1994, Non-universal scaling of fracture length and opening displacement: Nature, v. 367, p. 160–162, doi:10.1038/367160a0.

He, C., Z. Wang, and W. Yao (2007), Frictional sliding of gabbro gouge under hydrothermal conditions, *Tectonophysics*, *445*(3), 353-362, doi:https://doi.org/10.1016/j.tecto.2007.09.008.

He, C., W. Yao, Z. Wang, and Y. Zhou (2006), Strength and stability of frictional sliding of gabbro gouge at elevated temperatures, *Tectonophysics*, *427*(1), 217-229, doi:https://doi.org/10.1016/j.tecto.2006.05.023.

Ikari, M. J., C. Marone, and D. M. Saffer (2011), On the relation between fault strength and frictional stability, *Geology*, *39*(1), 83-86, doi:10.1130/g31416.1.

Ikari, M. J., C. Marone, D. M. Saffer, and A. J. Kopf (2013), Slip weakening as a mechanism for slow earthquakes, *Nature Geoscience*, *6*(6), 468-472, doi:10.1038/ngeo1818.

Ikari, M. J., F. K. Wilckens, and D. M. Saffer (2020), Implications of basement rock alteration in the Nankai Trough, Japan for subduction megathrust slip behavior, *Tectonophysics*, *774*, 228275, doi:https://doi.org/10.1016/j.tecto.2019.228275.

Ito, Y., & Ikari, M. J. (2015). Velocity-and slip-dependent weakening in simulated fault gouge: Implications for multimode fault slip. *Geophysical Research Letters*, *42*(22), 9247-9254.

Iverson, R. M., Dzurisin, D., Gardner, C. A., Gerlach, T. M., LaHusen, R. G., Lisowski, M., ... & Vallance, J. W. (2006). Dynamics of seismogenic volcanic extrusion at Mount St Helens in 2004–05. *Nature*, *444*(7118), 439-443.

Karner, S. L., & Marone, C. (2001). Fractional restrengthening in simulated fault gouge: Effect of shear load perturbations. *Journal of Geophysical Research: Solid Earth*, *106*(B9), 19319-19337.

Kaneko, Y., Avouac, J. P., & Lapusta, N. (2010). Towards inferring earthquake patterns from geodetic observations of interseismic coupling. *Nature Geoscience*, *3*(5), 363-369, doi:10.1038/ngeo843.

Kelemen, P., Benson, S. M., Pilorgé, H., Psarras, P., & Wilcox, J. (2019). An overview of the status and challenges of CO2 storage in minerals and geological formations. *Frontiers in Climate*, *1*, 9.

Kendrick, J. E., Lavallée, Y., Ferk, A., Perugini, D., Leonhardt, R., & Dingwell, D. B. (2012). Extreme frictional processes in the volcanic conduit of Mount St. Helens (USA) during the 2004–2008 eruption. *Journal of Structural Geology*, *38*, 61-76.

Klein, F. W. (2016). Lithospheric flexure under the Hawaiian volcanic load: Internal stresses and a broken plate revealed by earthquakes. *Journal of Geophysical Research: Solid Earth*, *121*(4), 2400-2428.

Klein, F. W., Koyanagi, R. Y., Nakata, J. S., & Tanigawa, W. R. (1987). The seismicity of Kilauea's magma system. *Volcanism in Hawaii, 2*, 1019-1185.

Khodayar, M., & Einarsson, P. (2002). Strike-slip faulting, normal faulting, and lateral dike injections along a single fault: Field example of the Gljúfurá fault near a Tertiary oblique rift-transform zone, Borgarfjörður, west Iceland. *Journal of Geophysical Research: Solid Earth*, *107*(B5), ETG-5.

Kristmannsdóttir, H. (1979). Alteration of basaltic rocks by hydrothermal-activity at 100-300 C. In *Developments in sedimentology* (Vol. 27, pp. 359-367). Elsevier.

Lengliné, O., Marsan, D., Got, J. L., Pinel, V., Ferrazzini, V., & Okubo, P. G. (2008). Seismicity and deformation induced by magma accumulation at three basaltic volcanoes. *Journal of Geophysical Research: Solid Earth*, *113*(B12).

Lin, G., & Okubo, P. G. (2020). Seismic Evidence for a Shallow Detachment Beneath Kīlauea's South Flank During the 2018 Activity. *Geophysical Research Letters*, *47*(15), e2020GL088003.

Lockwood, J. P., J. J. Dvorak, T. T. English, R. Y. Koyanagi, A. T. Okamura, M. L. Summers, and W. R. Tanigawa (1987), Mauna-Loa 1974–1984: A decade of intrusive and extrusive activity, in Volcanism in Hawaii, U. S. Geol. Surv. Prof. Pap., 1350, 537 - 570.

Logan, J. M. (1979). Experimental studies of simulated gouge and their application to studies of natural fault zones. In *Proceedings of conference VIII-analysis of actual fault zones in bedrock* (pp. 305-343).

Logan, J. M., Dengo, C. A., Higgs, N. G., & Wang, Z. Z. (1992). Fabrics of experimental fault zones: Their development and relationship to mechanical behavior. In *International geophysics* (Vol. 51, pp. 33-67). Academic Press, doi: https://doi.org/10.1016/S0074-6142(08)62814-4.

Logan, J. M., and K. A. Rauenzahn (1987), Frictional dependence of gouge mixtures of quartz and montmorillonite on velocity, composition and fabric, *Tectonophysics*, *144*(1), 87-108, doi:https://doi.org/10.1016/0040-1951(87)90010-2.

Mair, K., and C. Marone (1999), Friction of simulated fault gouge for a wide range of velocities and normal stresses, *Journal of Geophysical Research: Solid Earth*, *104*(B12), 28899-28914, doi:10.1029/1999jb900279.

Marone, C. (1998a), The effect of loading rate on static friction and the rate of fault healing during the earthquake cycle, *Nature*, *391*(6662), 69-72, doi:10.1038/34157.

Marone, C. (1998b), Laboratory-derived friction laws and their application to seismic faulting, *Annual Review of Earth and Planetary Sciences*, *26*(1), 643-696, doi:10.1146/annurev.earth.26.1.643.

Marone, C., and S. J. D. Cox (1994), Scaling of rock friction constitutive parameters: The effects of surface roughness and cumulative offset on friction of gabbro, *pure and applied geophysics*, *143*(1), 359-385, doi:10.1007/BF00874335.

Marone, C., and B. Kilgore (1993), Scaling of the critical slip distance for seismic faulting with shear strain in fault zones, *Nature*, *362*(6421), 618-621, doi:10.1038/362618a0.

Marone, C., C. B. Raleigh, and C. H. Scholz (1990), Frictional behavior and constitutive modeling of simulated fault gouge, *Journal of Geophysical Research: Solid Earth*, *95*(B5), 7007-7025, doi:10.1029/JB095iB05p07007.

McGrail, B. P., Schaef, H. T., Ho, A. M., Chien, Y. J., Dooley, J. J., & Davidson, C. L. (2006). Potential for carbon dioxide sequestration in flood basalts. *Journal of Geophysical Research: Solid Earth*, *111*(B12).

McGrail, B. P., F. A. Spane, E. C. Sullivan, D. H. Bacon, and G. Hund (2011), The Wallula basalt sequestration pilot project, *Energy Procedia*, *4*, 5653-5660, doi:10.1016/j.egypro.2011.02.557.

Mitchell, E. K., Fialko, Y., & Brown, K. M. (2015). Frictional properties of gabbro at conditions corresponding to slow slip events in subduction zones. *Geochemistry, Geophysics, Geosystems*, *16*(11), 4006-4020, doi:10.1002/2015gc006093.

Moore, P., N. R. Iverson, and R. M. Iverson (2008), Frictional properties of the Mount St. Helens gouge, *A Volcano Rekindled: The Renewed Eruption of Mount St. Helens, 2004-2006*, *1750*, 415-424.

Nielsen, S., Spagnuolo, E., & Violay, M. (2012). Composite sample mount assembly (SAMOA): The ultimate sample preparation for rotary shear experiments. *INGV Rapporti Tecnici. ISSN*, 2039-741.

Niemeijer, A., Di Toro, G., Nielsen, S., & Di Felice, F. (2011). Frictional melting of gabbro under extreme experimental conditions of normal stress, acceleration, and sliding velocity. *Journal of Geophysical Research: Solid Earth*, *116*(B7), doi:10.1029/2010jb008181.

Niemeijer, A. R., and R. L. M. Vissers (2014), Earthquake rupture propagation inferred from the spatial distribution of fault rock frictional properties, *Earth and Planetary Science Letters*, *396*, 154-164, doi:https://doi.org/10.1016/j.epsl.2014.04.010.

Reidel, S. P., Camp, V. E., Tolan, T. L., Kauffman, J. D., & Garwood, D. L. (2013). Tectonic evolution of the Columbia River flood basalt province. *Geological Society of America Special Papers*, *497*, 293-324, doi:10.1130/2013.2497(12).

Reinen, L. A., and J. D. Weeks (1993), Determination of rock friction constitutive parameters using an iterative least squares inversion method, *Journal of Geophysical Research: Solid Earth*, *98*(B9), 15937-15950, doi:10.1029/93JB00780.

Rice, J. R., and A. L. Ruina (1983), Stability of Steady Frictional Slipping, *Journal of Applied Mechanics*, *50*(2), 343-349, doi:10.1115/1.3167042.

Richardson, E., and C. Marone (1999), Effects of normal stress vibrations on frictional healing, *Journal of Geophysical Research: Solid Earth*, *104*(B12), 28859-28878, doi:10.1029/1999jb900320.

Ruina, A. L. (1983), Slip instability and state variable friction laws, *Journal of Geophysical Research: Solid Earth*, *88*(B12), 10359-10370, doi:10.1029/JB088iB12p10359.

Saffer, D.M., Marone, C., (2003). Comparison of smectite- and illite-rich gouge frictional properties: application to the updip limit of the seismogenic zone along subduction megathrust. *Earth Planet. Sci. Lett.* (215), 219–235. https://doi.org/10.1016/S0012-821X(03)00424-2.

Samuelson, J., D. Elsworth, and C. Marone (2009), Shear-induced dilatancy of fluid-saturated faults: Experiment and theory, *Journal of Geophysical Research*, *114*(B12), doi:10.1029/2008jb006273.

Scholz, C. H. (2000), Evidence for a strong San Andreas fault, *Geology*, *28*(2), 163-166, doi:10.1130/0091-7613(2000)28<163:Efassa>2.0.Co;2.

Scholz, C. H. (2002), *The Mechanics of Earthquakes and Faulting*, 2 ed., Cambridge University Press, Cambridge, doi:DOI: 10.1017/CBO9780511818516.

Scholz, C., P. Molnar, and T. Johnson (1972), Detailed studies of frictional sliding of granite and implications for the earthquake mechanism, *Journal of geophysical research*, *77*(32), 6392-6406.

Scott, D. R., C. J. Marone, and C. G. Sammis (1994), The apparent friction of granular fault gouge in sheared layers, *Journal of Geophysical Research: Solid Earth*, *99*(B4), 7231-7246, doi:10.1029/93jb03361.

Scuderi, M. M., C. Collettini, C. Viti, E. Tinti, and C. Marone (2017), Evolution of shear fabric in granular fault gouge from stable sliding to stick slip and implications for fault slip mode, *Geology*, doi:10.1130/g39033.1.

Scuderi, M. M., A. R. Niemeijer, C. Collettini, and C. Marone (2013), Frictional properties and slip stability of active faults within carbonate–evaporite sequences: The role of dolomite and anhydrite, *Earth and Planetary Science Letters*, *369-370*, 220-232, doi:10.1016/j.epsl.2013.03.024.

Shimamoto, T., & Tsutsumi, A. (1994). A new rotary-shear high-speed frictional testing machine: Its basic design and scope of research (in Japanese with English abstract). *Journal of Tectonic Research Group of Japan*, *39*, 65–78.

Snæbjörnsdóttir, S. Ó., B. Sigfússon, C. Marieni, D. Goldberg, S. R. Gislason, and E. H. Oelkers (2020), Carbon dioxide storage through mineral carbonation, *Nature Reviews Earth & Environment*, *1*(2), 90-102, doi:10.1038/s43017-019-0011-8.

Tesei, T., B. M. Carpenter, C. Giorgetti, M. M. Scuderi, A. Sagy, P. Scarlato, and C. Collettini (2017), Friction and scale-dependent deformation processes of large experimental carbonate faults, *Journal of Structural Geology*, *100*, 12-23, doi:10.1016/j.jsg.2017.05.008.

Villani, F., Pucci, S., Azzaro, R. *et al.* Surface ruptures database related to the 26 December 2018, M_W 4.9 Mt. Etna earthquake, southern Italy *Sci Data* **7,** 42 (2020). https://doi.org/10.1038/s41597-020-0383-0

Violay, M., S. Nielsen, B. Gibert, E. Spagnuolo, A. Cavallo, P. Azais, S. Vinciguerra, and G. Di Toro (2014), Effect of water on the frictional behavior of cohesive rocks during earthquakes, *Geology*, *42*(1), 27-30, doi:10.1130/g34916.1.

Violay, M., S. Nielsen, E. Spagnuolo, D. Cinti, G. Di Toro, and G. Di Stefano (2013), Pore fluid in experimental calcite-bearing faults: Abrupt weakening and geochemical signature of co-seismic processes, *Earth and Planetary Science Letters*, *361*, 74-84, doi:10.1016/j.epsl.2012.11.021.

Walker, R. J., R. E. Holdsworth, P. J. Armitage, and D. R. Faulkner (2013a), Fault zone permeability structure evolution in basalts, *Geology*, *41*(1), 59-62, doi:10.1130/g33508.1.

Walker, R., R. Holdsworth, J. Imber, and D. Ellis (2012), Fault-zone evolution in layered basalt sequences: A case study from the Faroe Islands, NE Atlantic margin, *Geological Society of America Bulletin*, *124*, 1382-1393, doi:10.1130/B30512.1.

Walker, R. J., R. E. Holdsworth, J. Imber, D. R. Faulkner, and P. J. Armitage (2013b), Fault zone architecture and fluid flow in interlayered basaltic volcaniclastic-crystalline sequences, *Journal of Structural Geology*, *51*, 92-104, doi:https://doi.org/10.1016/j.jsg.2013.03.004.

Weeks, J. D. (1993), Constitutive laws for high-velocity frictional sliding and their influence on stress drop during unstable slip, *Journal of Geophysical Research: Solid Earth*, *98*(B10), 17637-17648, doi:10.1029/93JB00356.

Wong, T.-f., Y. Gu, T. Yanagidani, and Y. Zhao (1992), Chapter 5 Stabilization of Faulting by Cumulative Slip, in *International Geophysics*, edited by B. Evans and T.-f. Wong, pp. 119-143, Academic Press, doi:https://doi.org/10.1016/S0074-6142(08)62820-X.

Zhang, L., C. He, Y. Liu, and J. Lin (2017), Frictional properties of the South China Sea oceanic basalt and implications for strength of the Manila subduction seismogenic zone, *Marine Geology*, *394*, 16-29, doi:10.1016/j.margeo.2017.05.006.

EXPERIMENT NAME			CONDITIONS	SLIP (mm)	(MPa)	(MPa)		Velocity Steps (μm/s)	hold times (s)	ear strain (-)/ slip (mm)
b817	BRAVA	Simulated gouge	Room-dry	6	5	3.14	0.63	0.1-0.3-1-3-10-30-100-300	30-100-300-1000-3000	3.8/14.1
b818	BRAVA	Simulated gouge	Room-dry	6	10	6.17	0.62	0.1-0.3-1-3-10-30-100-300	30-100-300-1000-3000	4.3/14.2
b819	BRAVA	Simulated gouge	Room-dry	6	20	12.54	0.63	0.1-0.3-1-3-10-30-100-300	30-100-300-1000-3000	4.3/14.1
b820	BRAVA	Simulated gouge	Room-dry	6	30	18.78	0.63	0.1-0.3-1-3-10-30-100-300	30-100-300-1000-3000	4.2/15.1
b821	BRAVA	Simulated gouge	Wet	7	5	3.15	0.63	0.1-0.3-1-3-10-30-100-300	30-100-300-1000-3000	4.2/15.1
b822	BRAVA	Simulated gouge	Wet	7	10	6.09	0.61	0.1-0.3-1-3-10-30-100-300	30-100-300-1000-3000	4.7/15.1
b823	BRAVA	Simulated gouge	Wet	7	20	12.42	0.62	0.1-0.3-1-3-10-30-100-300	30-100-300-1000-3000	4.7/15.1
b824	BRAVA	Simulated gouge	Wet	7	30	18.69	0.62	0.1-0.3-1-3-10-30-100-300	30-100-300-1000-3000	4.5/15.1
b840	BRAVA	Bare surfaces (slabs)	Room-dry	3	5	3.78	0.76	0.1-0.3-1-3-10-30-100-300	30-100-300-1000-3000	-/10.6
b844	BRAVA	Bare surfaces (slabs)	Room-dry	3	7.5	5.83	0.78	0.1-0.3-1-3-10-30-100-300	30-100-300-1000-3000	-/10.7
b841	BRAVA	Bare surfaces (slabs)	Room-dry	3	10	7.72	0.77	0.1-0.3-1-3-10-30-100-300	30-100-300-1000-3000	-/10.6
b842	BRAVA	Bare surfaces (slabs)	Wet	3	5	3.61	0.72	0.1-0.3-1-3-10-30-100-300	30-100-300-1000-3000	-/10.7
b843	BRAVA	Bare surfaces (slabs)	Wet	3	10	7.44	0.74	0.1-0.3-1-3-10-30-100-300	30-100-300-1000-3000	-/10.6

Table 1: List of BRAVA experiments and summary of experimental conditions. All experiments were sheared run-in at a sliding velocity of 10 μm/s. Acronyms and symbols: RI = "run-in" phase; σ_n = normal stress; τ_{ss} = shear stress at steady state; μ_{ss} = coefficient of stable sliding friction at steady state. τ_{ss} and μ_{ss} are both recorded at the end of the run-in phase.

EXPERIMENT NAME			CONDITIONS	(mm)	(MPa)	(MPa)		hold times (s)	strain (-)/ slip (mm)
s1658	SHIVA	Bare surfaces (cylinders)	Room-dry	4 - 56	3.93 - 4.21	2.27 - 2.71	0.58 - 0.64	120	-/56
s1624	SHIVA	Bare surfaces (cylinders)	Room-dry	4 - 56	7.92 - 7.89	5.18 - 5.44	0.65 - 0.69	-	-/56
s1626	SHIVA	Bare surfaces (cylinders)	Room-dry	4 - 56	7.92 - 7.83	5.06 - 5.60	0.64 - 0.72	120	-/56
s1657	SHIVA	Bare surfaces (cylinders)	Room-dry	4 - 56	12.25 - 12.29	8.22 - 9.08	0.67 - 0.74	120	-/56
s1627	SHIVA	Bare surfaces (cylinders)	Wet	4 - 56	7.94 - 7.87	5.00 - 5.60	0.63 - 0.71	-	-/56
s1662	SHIVA	Bare surfaces (cylinders)	Wet	4 - 56	3.83 - 3.63	1.97 - 2.13	0.51 - 0.59	120	-/56
s1633	SHIVA	Bare surfaces (cylinders)	Wet	4 - 56	7.94 - 7.83	4.97 - 5.38	0.59 - 0.68	120	-/56
s1661	SHIVA	Bare surfaces (cylinders)	Wet	4 - 56	12.10 - 12.04	7.24 - 8.64	0.60 - 0.72	120	-/56

Table 2: List of SHIVA experiments and summary of experimental conditions. All experiments were sheared run-in at a sliding velocity of 10 µm/s for 2 mm slip. Acronyms and symbols: σ_n = normal stress; τ_{ss} = shear stress at steady state; μ_{ss} = coefficient of stable sliding friction at steady state. τ_{ss} and μ_{ss} are both recorded after net slip of 4 mm and 56 mm, respectively.

NAME		conditions	(MPa)	from 0.1 to 300 µm/s	interval vel steps	Rate, ß	interval slide-hold-slides
b817	BRAVA	Room-dry	5	-0.000099 to 0.000622	7.1-10.7/1.8-2.8	0.0055	11.6-14.1/3.0-3.8
b818	BRAVA	Room-dry	10	0.000076 to -0.002009	7.2-10.8/2.0-3.2	0.0063	11.7-14.2/3.5-4.3
b819	BRAVA	Room-dry	20	-0.000019 to -0.000983	7.1-10.7/2.0-3.2	0.0056	11.6-14.1/3.5-4.3
b820	BRAVA	Room-dry	30	0.000408 to 0.000021	8.1-11.7/2.1-3.1	0.0051	12.6-15.1/3.4-4.2
b821	BRAVA	Wet	5	0.000254 to 0.001988	8.1-11.7/2.1-3.1	0.0091	12.6-15.1/3.4-4.2
b822	BRAVA	Wet	10	0.000216 to -0.001368	8.1-11.7/2.3-3.5	0.0124	12.6-15.1/3.8-4.7
b823	BRAVA	Wet	20	0.000878 to -0.000333	8.1-11.7/2.3-3.5	0.0127	12.6-15.1/3.8-4.7
b824	BRAVA	Wet	30	0.000787 to -0.000377	8.0-11.6/2.2-3.3	0.0128	12.6-15.1/3.6-4.5
b840	BRAVA	Room-dry	5	-0.007459 to 0.005931	3.6-7.2/-	0.0241	8.1-10.6/-
b844	BRAVA	Room-dry	7.5	-0.000278 to 0.007392	3.6-7.2/-	0.0265	8.1-10.6/-
b841	BRAVA	Room-dry	10	-0.005408 to 0.006239	3.6-7.2/-	0.0236	8.2-10.7/-
b842	BRAVA	Wet	5	-0.01196 to 0.000691	3.5-7.1/-	0.0211	8.1-10.6/-
b843	BRAVA	Wet	10	-0.009932 to 0.002302	3.6-7.2/-	0.0244	8.2-10.7/-

Table 3: Summary of the velocity stepping and slide-hold-slide tests. Acronyms and symbols: σ_n = normal stress.

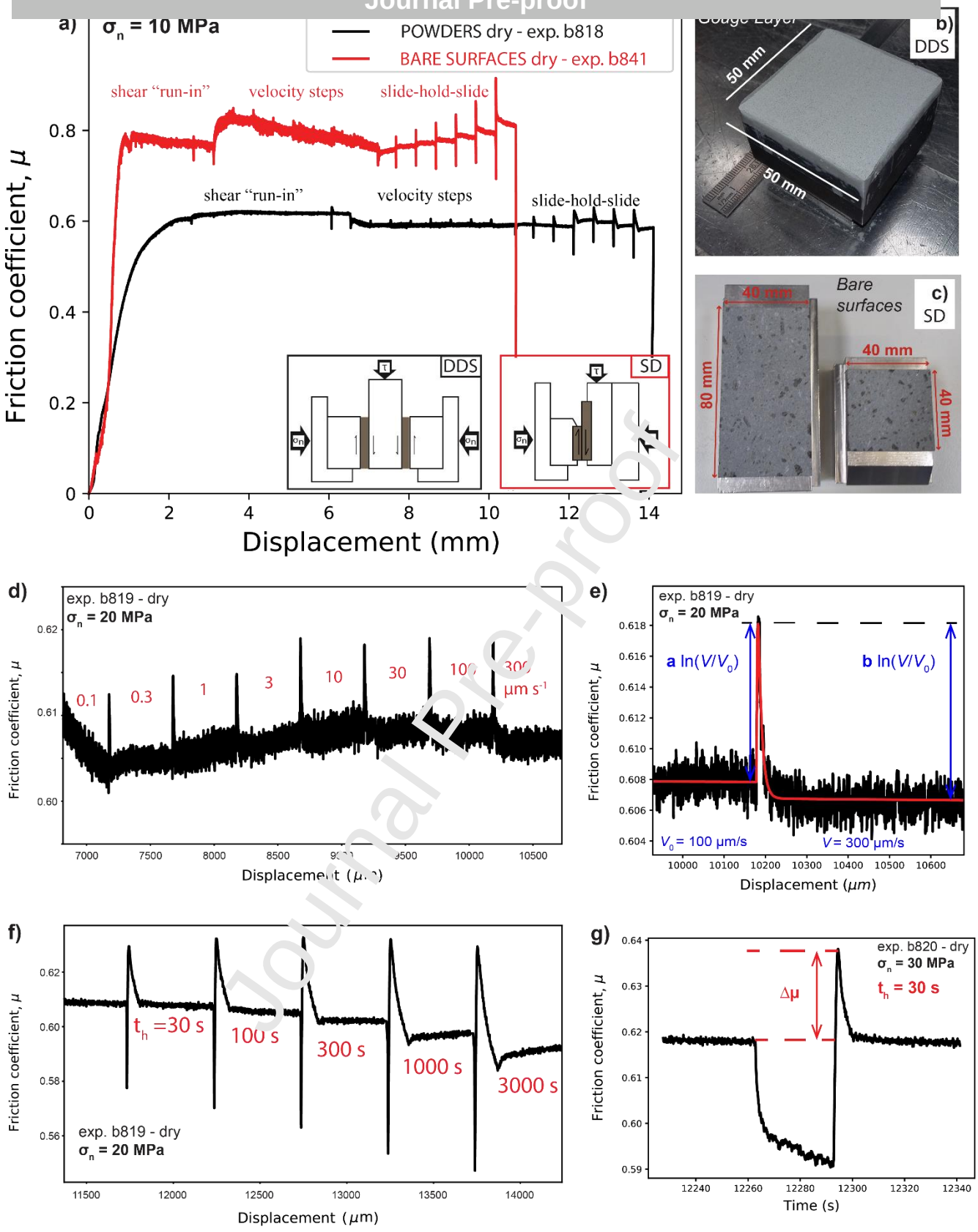

Figure 1. (a) Friction vs. displacement curves retrieved from two typical direct shear experiments involving simulated fault gouge (black line) and bare surfaces (red line). **(b)** Double direct shear, DDS, configuration for the simulated fault gouge and the single direct, SD, shear configuration for bare rock surfaces **(c).** The "shear run-in" phase is conceived to attain a steady-state friction condition and precedes the velocity step and slide-hold-hold sequences. **(d)**

Fricti y step modeled with a fifth order Runge Kutta numerical integration. The "direct effect" *a* scales as the sudden change in friction upon the velocity upstep and the "evolution effect" *b* scales as the subsequent decay in friction towards a new steady-state value. **(f)** Friction vs. displacement for a representative slide-hold-slide sequence. t_h denotes the hold time. **(g)** Friction vs. time for a 30 s hold. Frictional healing Δμ is measured as the difference between peak friction value upon re-shear and the pre-hold steady-state friction.

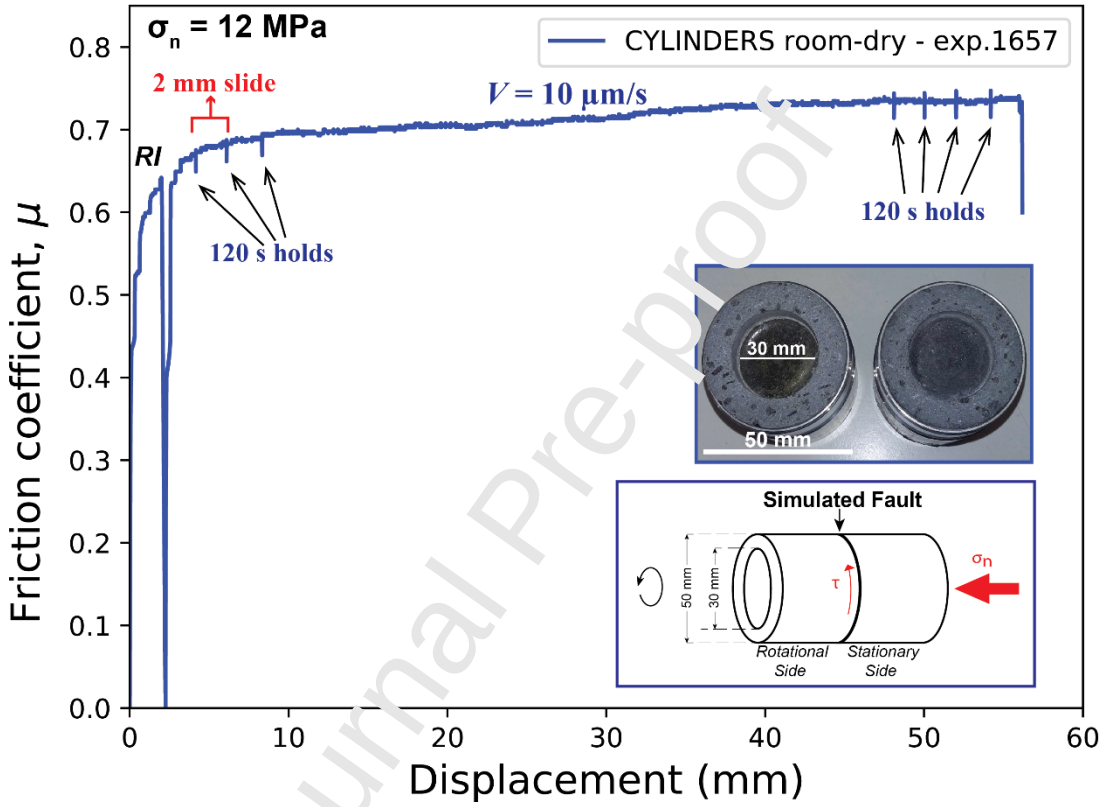

Figure 2. Friction against displacement curve in a typical test performed on basalt hollow cylinders with the rotary-shear apparatus SHIVA. The sequences of 2 mm sliding at 10 µm/s followed by 120 s holds were reiterated to interrogate the frictional strength evolution within small displacement intervals. RI denotes the "shear run-in" phase.

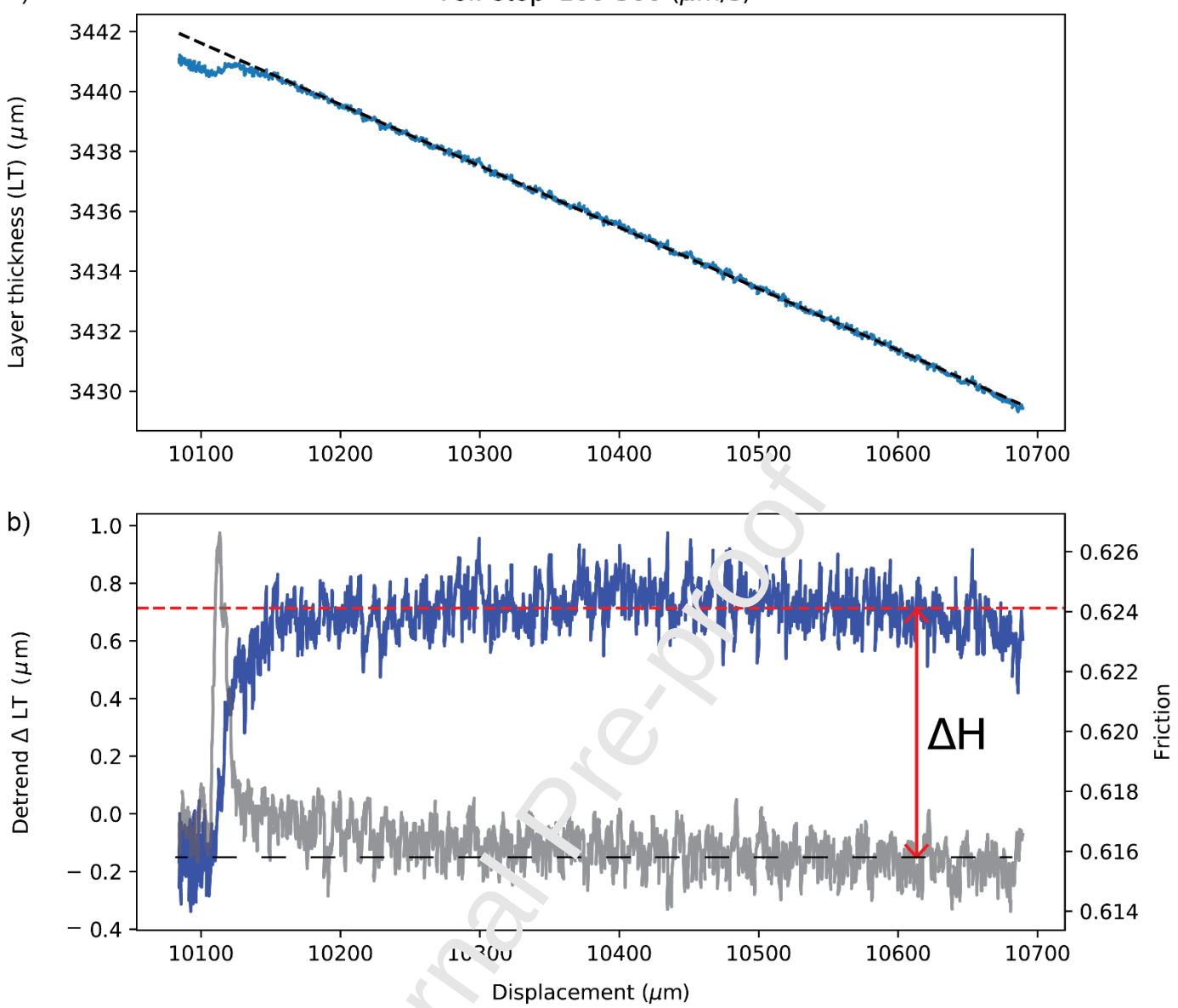

Figure 3. (a) Raw layer thickness data for the analyzed 100-300 μm/s velocity step. The dashed black straight line is the trend originated from the geometrical layer thinning throughout the test that is to be removed ahead of the dilation analysis. **(b)** Enlargement of the velocity step (gray line) and the accompanying gouge layer dilation (blue line) recorded by the horizontal LVDT. The steady-state dilation, ΔH, is measured as the difference between the layer thickness upon the new steady-state friction, averaged over the displacement cumulated during the velocity segment (dashed red line), and the average layer thickness prior to the velocity upstep.

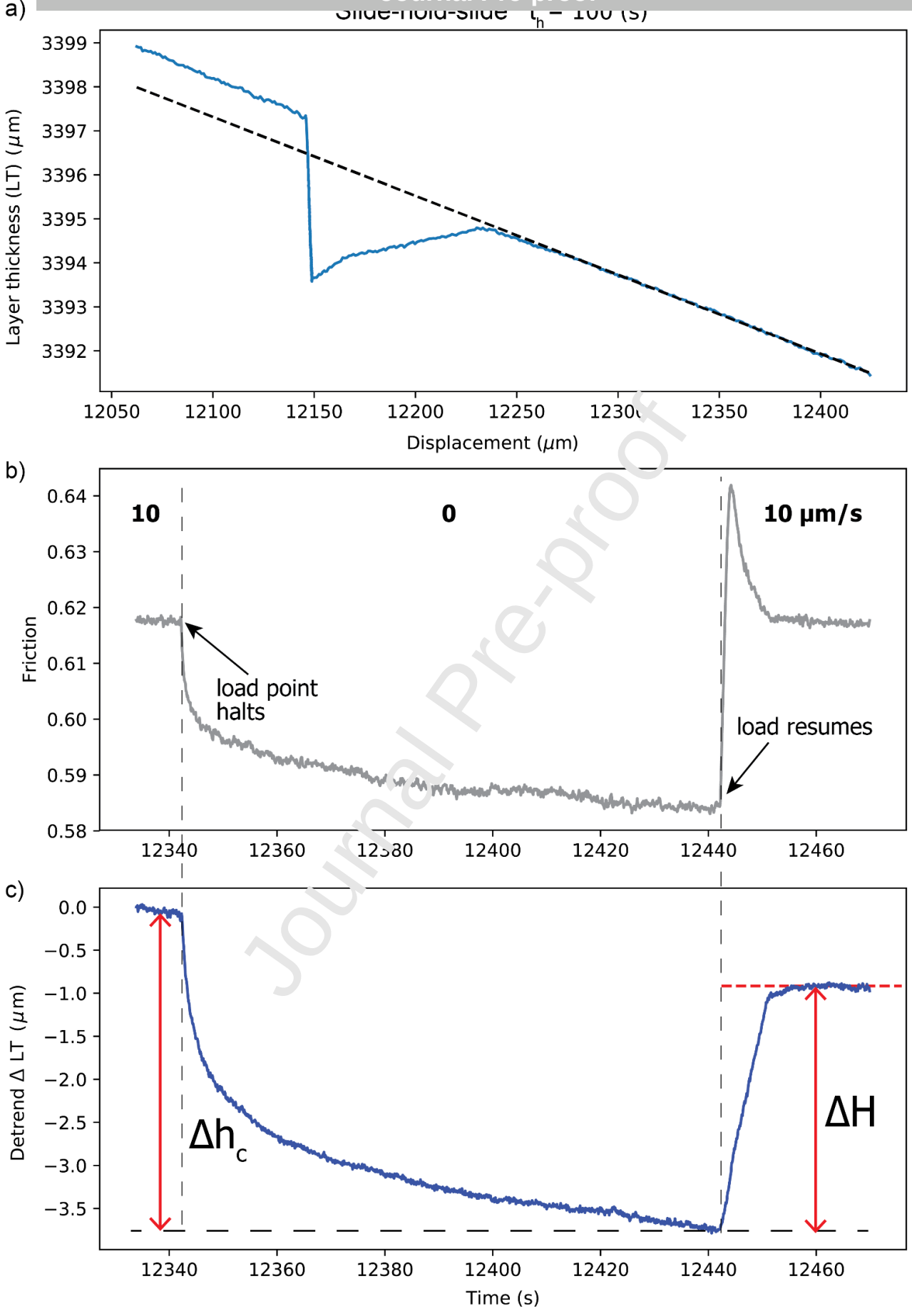

Figu s, and the associated negative linear trend (dashed black line) due to geometrical layer thinning. **(b)** Friction variations with time during the selected slide-hold-slide segment and **(c)** the related volumetric response of the gouge layer after detrending the layer thickness data, using the same approach outlined for the velocity steps. Δh_c indicates the volumetric compaction accompanying the hold phase, defined as the difference between the layer thickness just before and at the end of the hold period; whereas ΔH is the steady-state dilation occurring as load resumes, calculated as the difference between the average layer thickness following re-shear at steady-state friction (dashed red line) and the layer thickness at the end of the hold period.

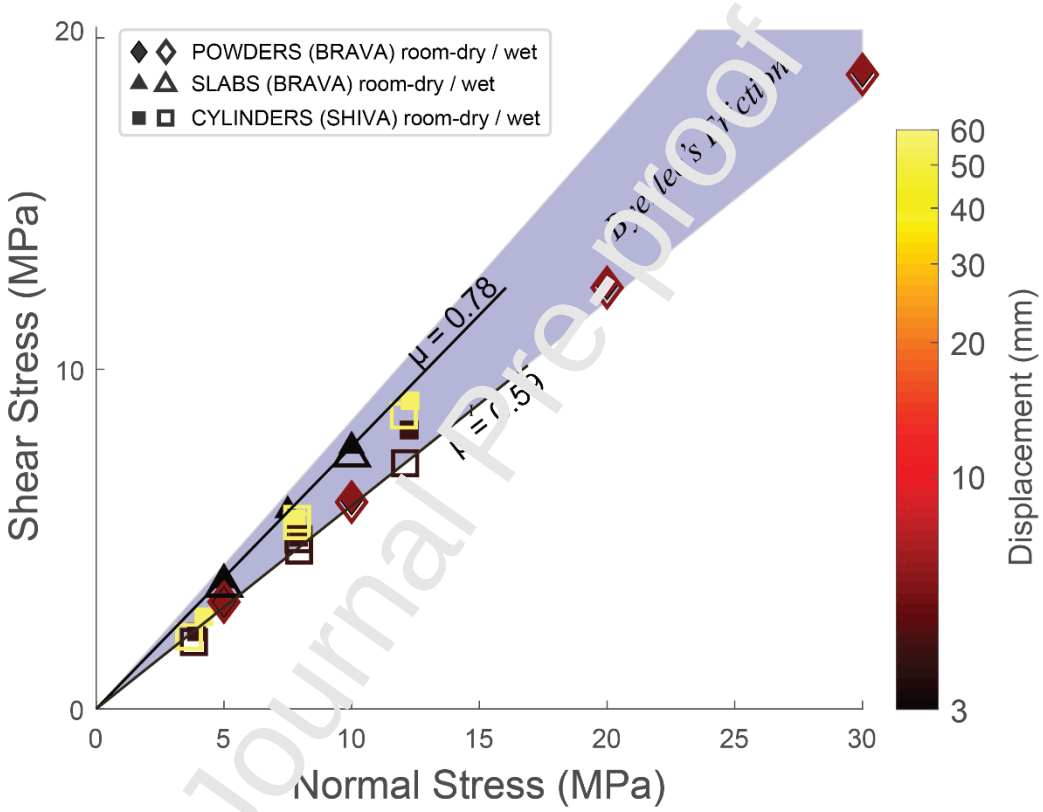

Figure 5. Mohr-Coulomb failure diagram reporting the compilation of shear strength values collected at different normal stresses. The linear reactivation envelopes fall within the field of Byerlee's friction law (i.e., μ = 0.6 – 0.85, shaded area), regardless of tested samples, shear configuration, and environmental conditions.

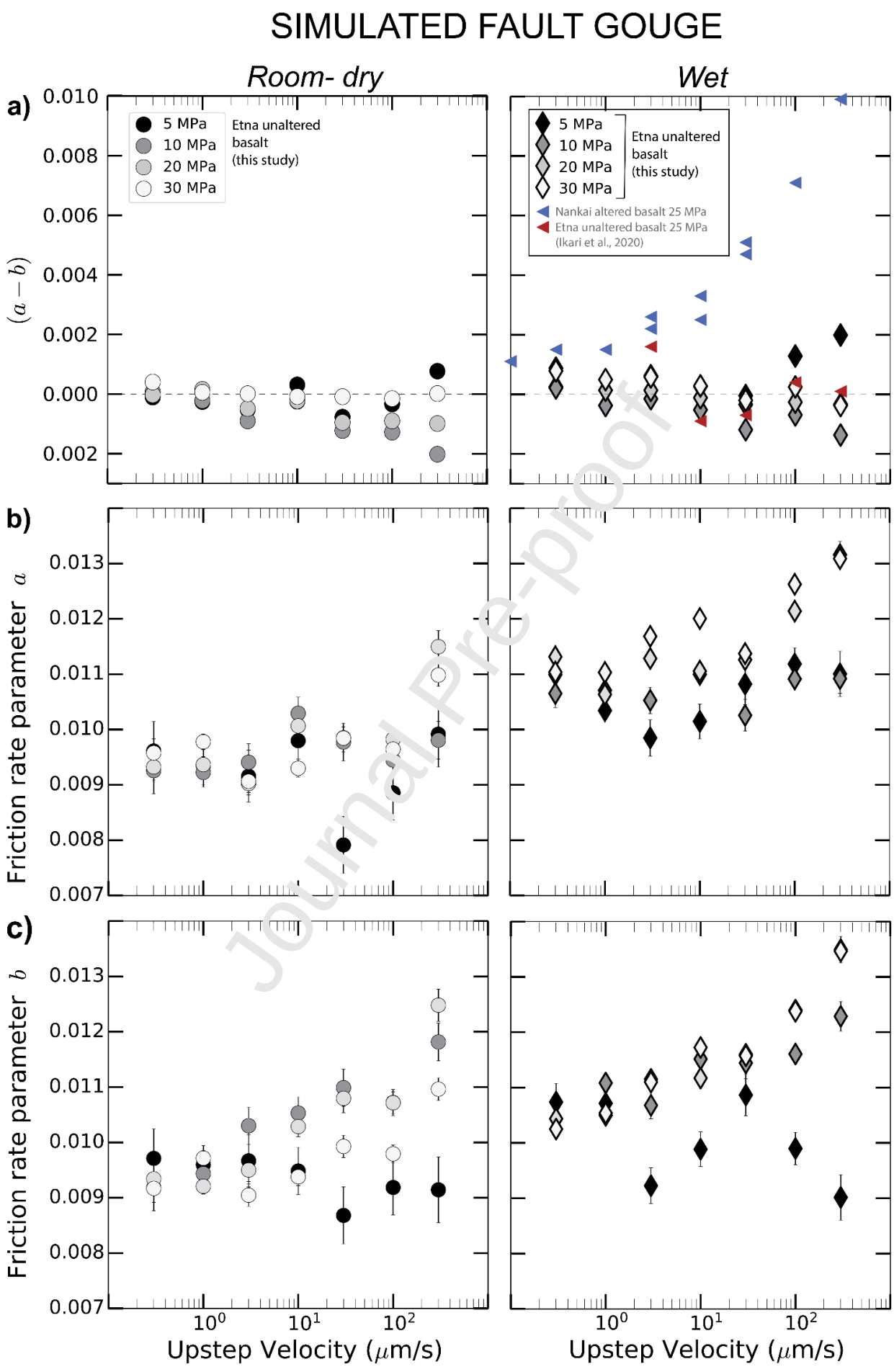

Figure 6. Results from velocity stepping tests in simulated fault gouge deformed at 5 to 30 MPa normal stress, under room-dry and wet conditions. **(a)** Friction velocity dependence *(a-b)* and the associated friction rate parameters *a* **(b)** and *b* **(c)** as a function of the velocity upsteps.

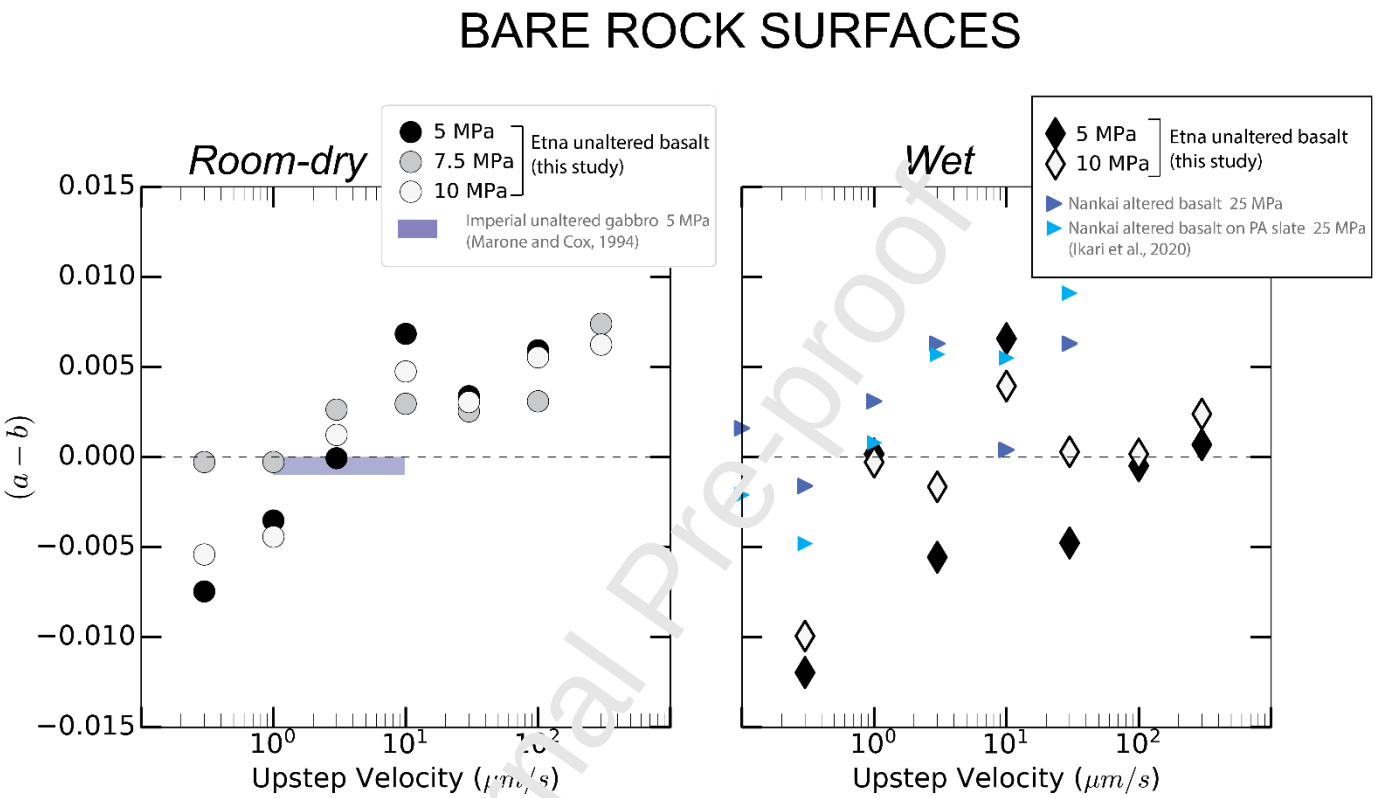

Figure 7. Results from velocity stepping tests in bare rock surfaces deformed at 5 to 10 MPa normal stress, under room-dry and wet conditions. Evolution of the friction constitutive parameter *(a-b)* plotted against the velocity upsteps.

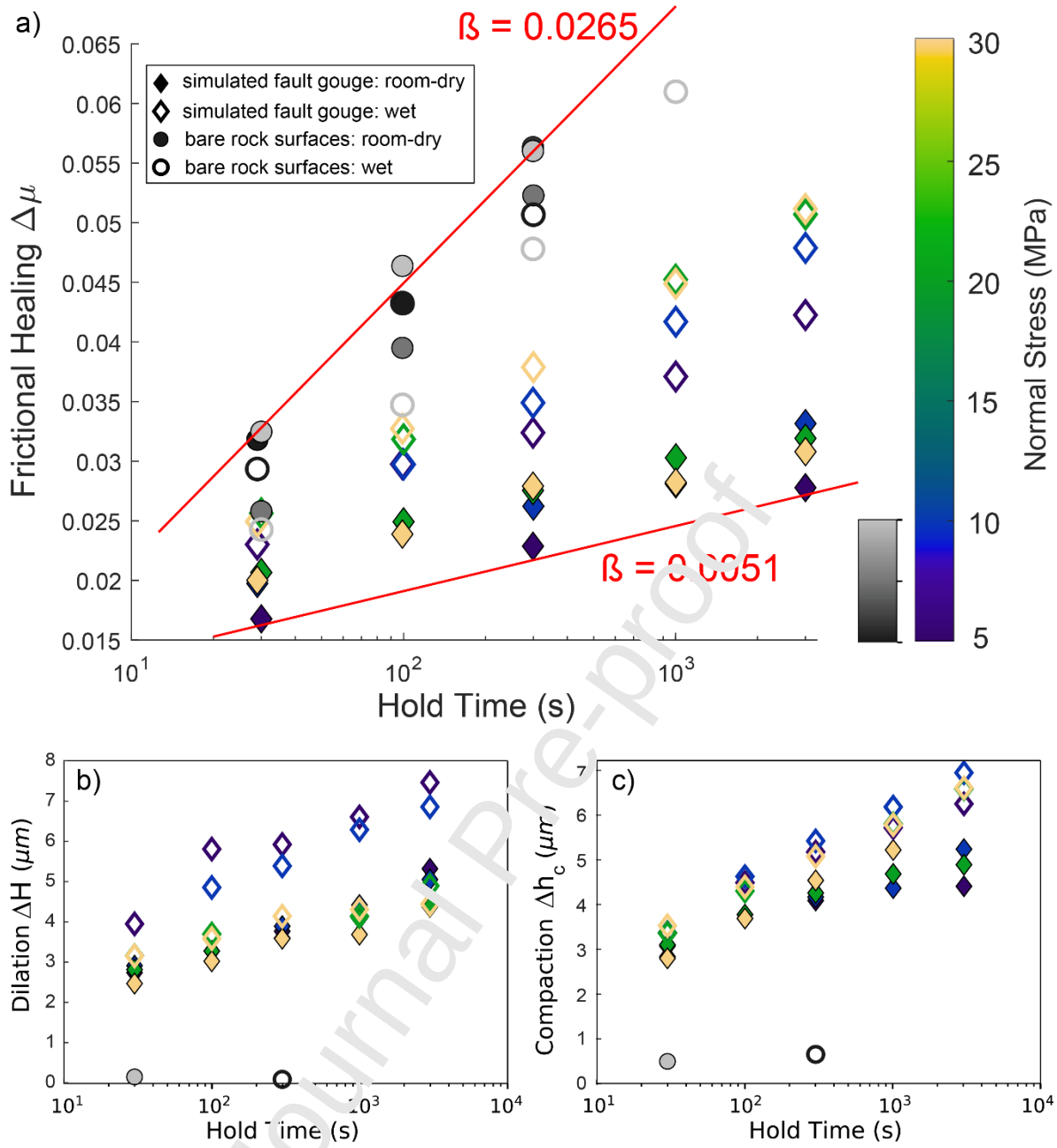

Figure 8. (a) Frictional healing parameter Δμ plotted against the hold time, t_h, for each experimental configuration. Two populations of healing rates, ß, can be observed: lower healing rates for synthetic fault gouge and higher rates for bare rock surfaces. **(b)** Positive dilation and **(c)** compaction rates accompany the time-dependent friction restrengthening during slide-hold-slide tests.

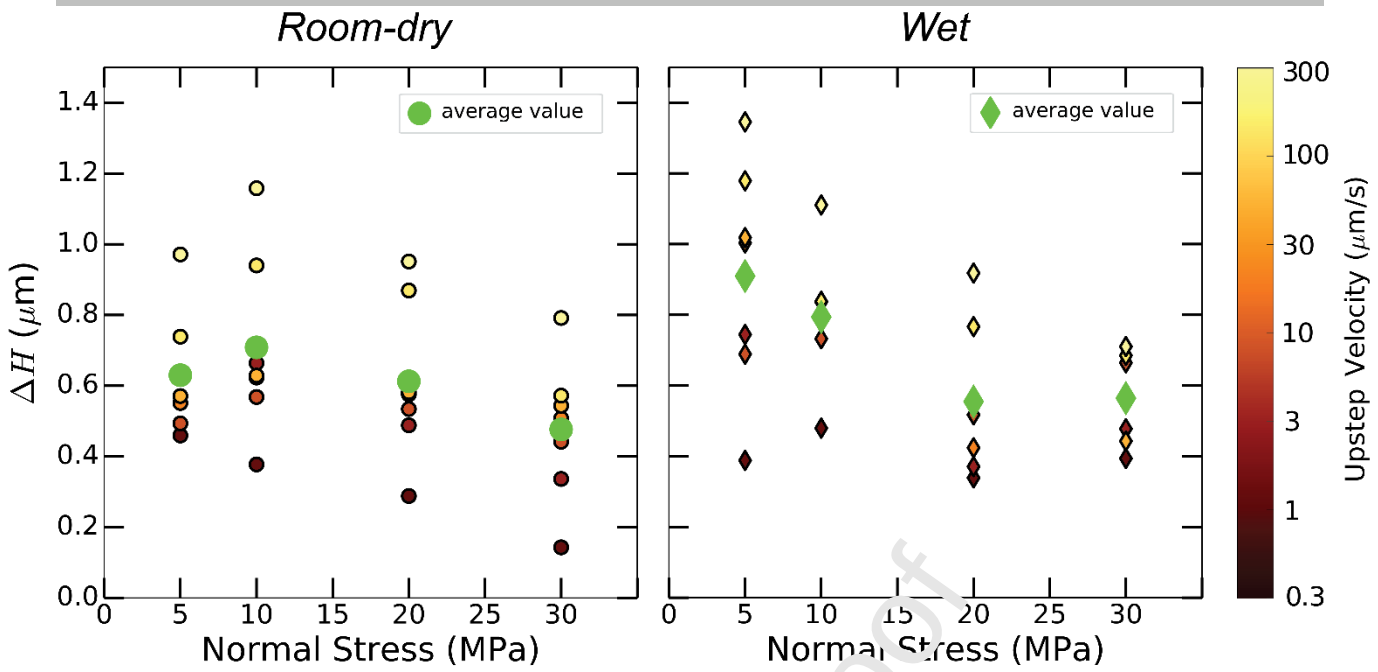

Figure 9. Steady-state dilation, ΔH, as a function of the normal stress and the velocity upsteps. Green symbols represent the ΔH values averaged over the entire velocity step sequence 0.1-300 μm/s at a given normal stress.

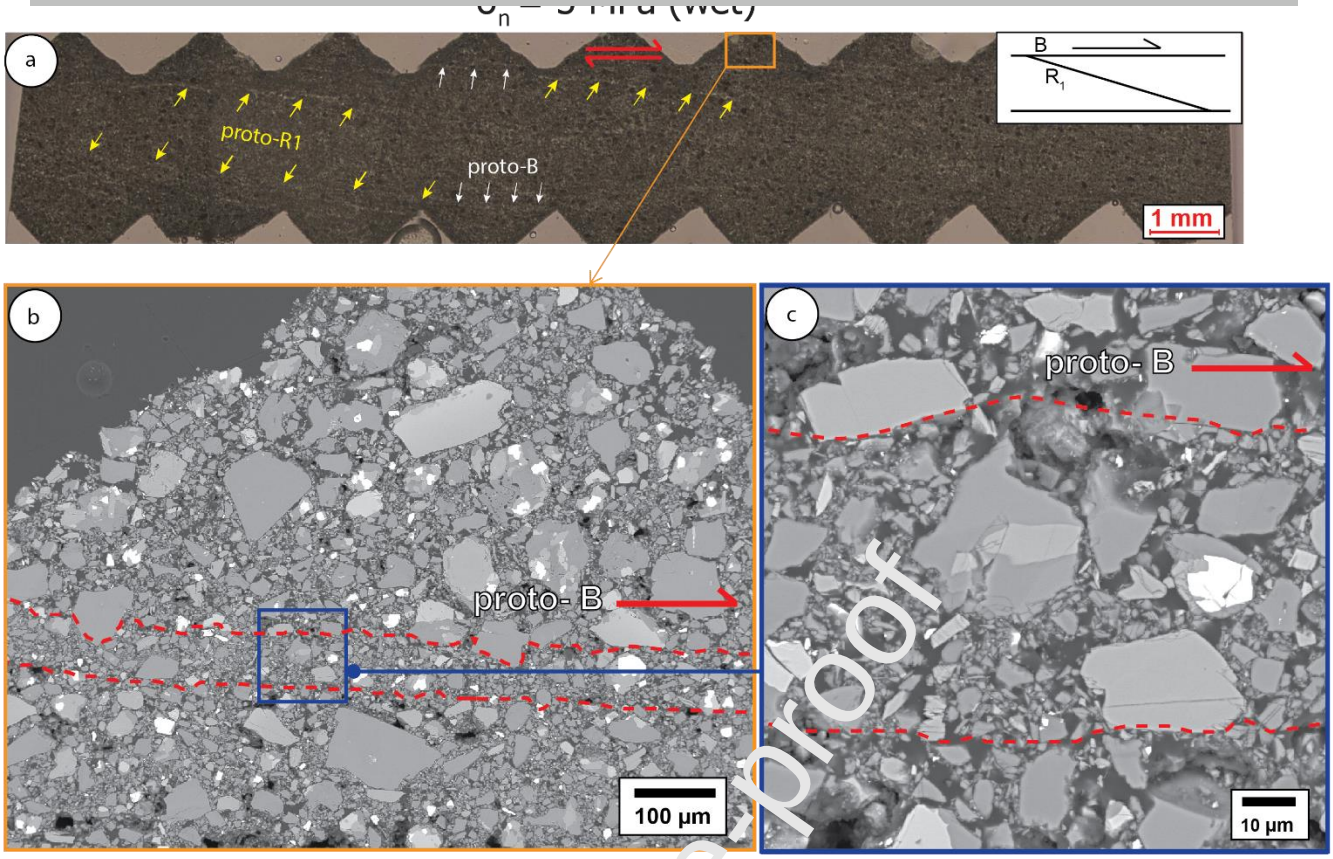

Figure 10. (a) Optical microscope picture of a simulated basalt fault gouge deformed at low normal stress under wet conditions. The sense of shear is shown by the red arrows. The yellow and white arrows highlight, respectively, the trace of some proto-R1 and proto-B shear bands. **(b)** Back-scattered image of the proto-boundary shear zone and **(c)** enlargement within the proto-B showing details of the shear band microstructure.

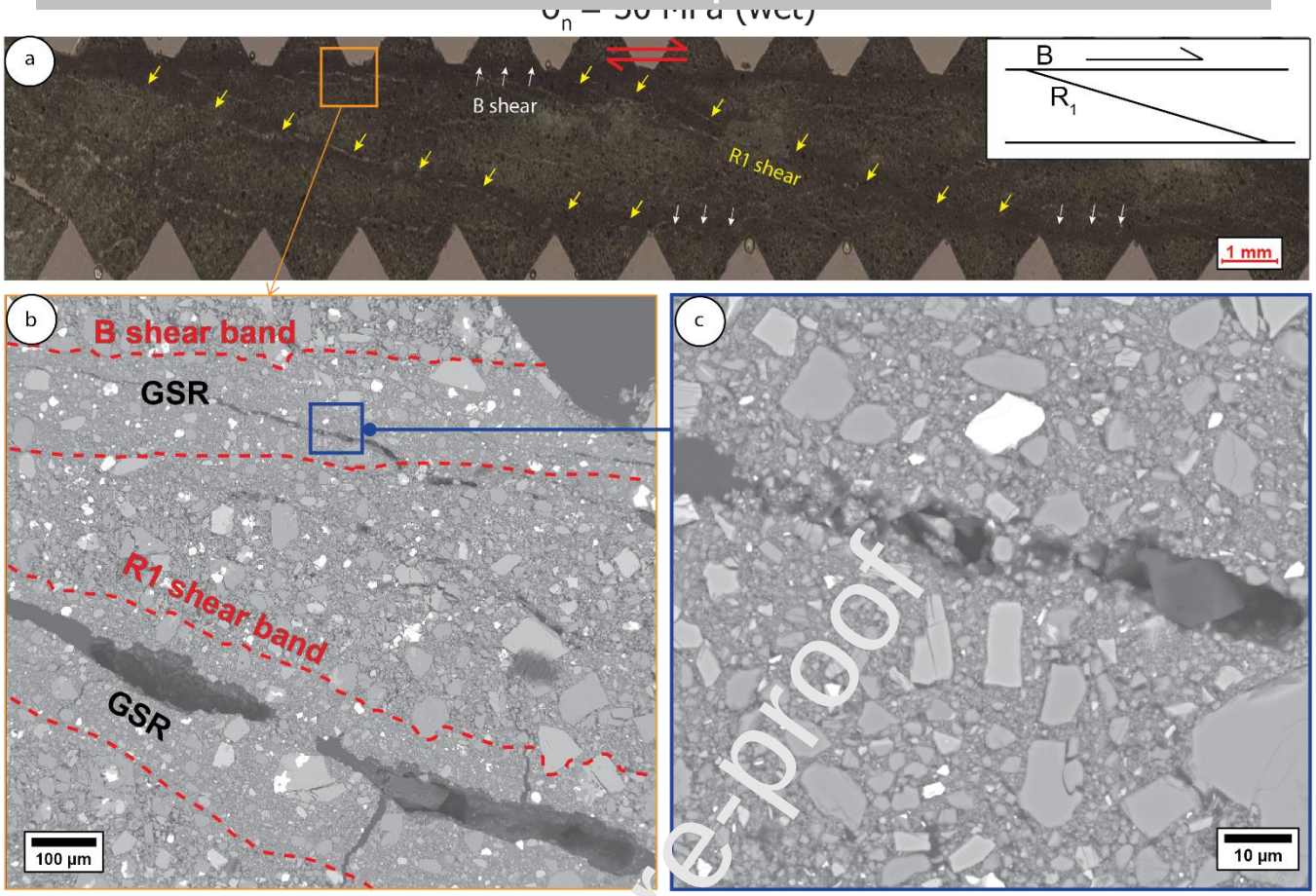

Figure 11. (a) Micrograph of a basalt layer deformed at 30 MPa normal stress under wet conditions. The sense of shear is shown by the red arrows. The yellow and white arrows depict, respectively, the trace of some well-developed R1 and B shear bands. **(b)** Backscatter scanning electron (SEM) image highlighting the R1 and B shear bands characterized by enhanced grain size reduction (GSR). **(c)** Enlargement of a B-shear zone representing the prominent microstructure of a typical localized shear zone observed at $\sigma_n \geq 10$ MPa.

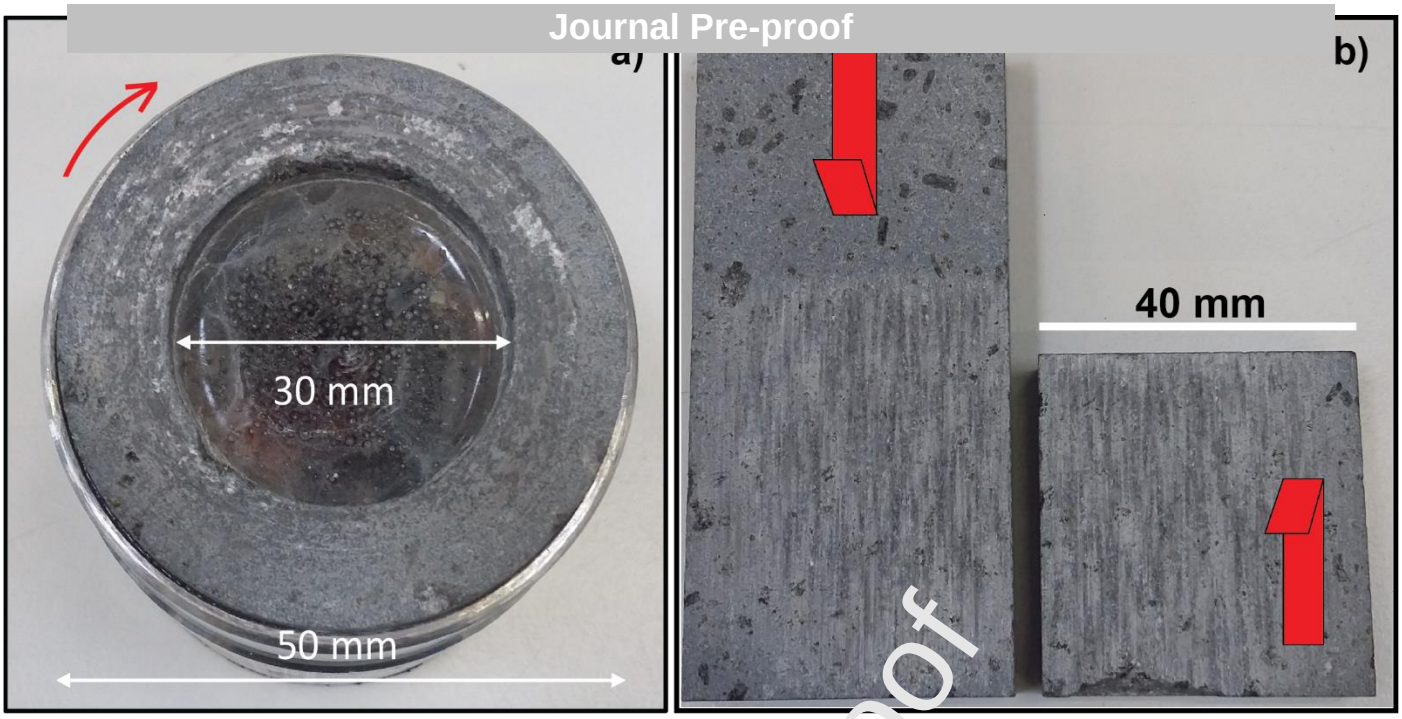

Figure 12. Microstructures of post-tested simulated basalt fault surfaces with their characteristic frictional wearing features. The bare surfaces were deformed at σ_n = 8 MPa **(a)** and 10 MPa **(b)** under room-dry conditions, in a rotary-shear **(a)** and direct shear **(b)** configuration.

HIGHLIGHTS

- Unaltered basalt faults are frictionally strong with high healing rates
- Basalt microstructural heterogeneities affect the stability of sliding
- Fault gouges may nucleate slip instabilities
- Bare rock surfaces are less prone to unstable slip